University of Alberta

Investigating the Performance of an Aerated Grit Chamber

by

Afsana Habib

A thesis submitted to the Faculty of Graduate Studies and Research
in partial fulfillment of the requirements for the degree of

Master of Science
in
Environmental Engineering

Department of Civil and Environmental Engineering

Edmonton, Alberta
Fall 2008

Library and Archives Canada

Published Heritage Branch

395 Wellington Street
Ottawa ON K1A 0N4
Canada

Bibliothèque et Archives Canada

Direction du Patrimoine de l'édition

395, rue Wellington
Ottawa ON K1A 0N4
Canada

Your file Votre référence
ISBN: 978-0-494-47258-3
Our file Notre référence
ISBN: 978-0-494-47258-3

NOTICE:
The author has granted a non-exclusive license allowing Library and Archives Canada to reproduce, publish, archive, preserve, conserve, communicate to the public by telecommunication or on the Internet, loan, distribute and sell theses worldwide, for commercial or non-commercial purposes, in microform, paper, electronic and/or any other formats.

The author retains copyright ownership and moral rights in this thesis. Neither the thesis nor substantial extracts from it may be printed or otherwise reproduced without the author's permission.

AVIS:
L'auteur a accordé une licence non exclusive permettant à la Bibliothèque et Archives Canada de reproduire, publier, archiver, sauvegarder, conserver, transmettre au public par télécommunication ou par l'Internet, prêter, distribuer et vendre des thèses partout dans le monde, à des fins commerciales ou autres, sur support microforme, papier, électronique et/ou autres formats.

L'auteur conserve la propriété du droit d'auteur et des droits moraux qui protège cette thèse. Ni la thèse ni des extraits substantiels de celle-ci ne doivent être imprimés ou autrement reproduits sans son autorisation.

In compliance with the Canadian Privacy Act some supporting forms may have been removed from this thesis.

While these forms may be included in the document page count, their removal does not represent any loss of content from the thesis.

Conformément à la loi canadienne sur la protection de la vie privée, quelques formulaires secondaires ont été enlevés de cette thèse.

Bien que ces formulaires aient inclus dans la pagination, il n'y aura aucun contenu manquant.

Canada

ABSTRACT

In this work, a pilot-scale aerated grit chamber model was designed and constructed to replicate the full-scale unit at Gold Bar wastewater treatment plant. The model was built to a 15:1 scale based on Froude number similitude criterion. Tracer studies were conducted on the pilot-scale unit to investigate the flow pattern inside the chamber. The non-ideal flow pattern was best described by nine-tanks in series model. Grit samples were collected around the full-scale grit chamber and analyzed to evaluate the tank's performance and the grit's properties. A pilot-scale mixing tank was specially designed and built to perform baseline study of the effect of using hydraulic jets in grit chamber operation. Planar laser induced fluorescence technique was employed to investigate the flow pattern inside the tank and jet-mixing phenomena. The analyses indicated highest axial dispersion was achieved inside the tank with four jet-injectors.

ACKNOWLEDGEMENTS

First and foremost I would like to express sincere gratitude to my supervisor Dr. M. Gamal El-Din, who has the attitude and essence of a genius. He continually conveyed a spirit of excitement and adventure all through my research and graduate studies. I would also like to express deepest appreciation to my co-supervisor Dr. I.D. Buchanan for his support, guidance and encouragement. My sincere gratitude goes to Dr. M.S.A. Baawain for his thoughtful advice which often served to give me a sense of direction in my research. He had been abundantly helpful in providing hands-on training on laser.

I would like to thank Darryl Seehagel and Bilgin Buberoglu at Edmonton Waste Management Center of Excellence for their input in acquiring design and operational data from Gold Bar WWTP. My special thanks to Maria Demeter for her help during sample collection and to Nick Chernuka for taking care of all the plumbing works. A very special thanks goes to Dr. K. Ikehata for the encouragements he offered during my stay at the University. Thanks to Atefeh, Ding, Helen and Mohua for all the coffee breaks over the past two years. I wish them all the best in future.

I am forever grateful to my parents, Ahsan and Rownak Habib, and my bro Aurin for letting me disappear for the past two years. A very special gratitude goes to my uncles and my mother-in-law Tahmina Banu for believing in me always.

Finally I would like to mention my beloved husband Saif Molla. Without him it would not have been possible for me to finish my research. Thanks for sticking by my side, even when I was irritable and depressed. This thesis is a small tribute to this exceptional man of my life.

TABLE OF CONTENTS

Chapter 1 Introduction

1.1 Problem Background 1
1.2 Preliminary Treatment at Gold Bar Wastewater Treatment Plant 2
1.3 Aerated Grit Chamber 4
1.4 Scope of the Thesis 5

Chapter 2 Design of Pilot-scale Aerated Grit Chamber

2.1 Introduction 8
2.2 Similitude 8
2.2.1 Geometric Similitude 8
2.2.2 Kinematic Similitude 9
2.2.3 Dynamic Similitude 9
2.3 Dynamic Similitude Criterion 9
2.4 Pilot-scale Model Design Strategy 12
2.4.1 Full-scale Aerated Grit Chamber at Gold Bar WWTP 12
2.4.2 Hydraulic Considerations of Full-scale Aerated Grit Chamber 13
2.4.3 Dynamic Similitude Criterion 15
2.4.4 Scale Factor 16
2.4.5 Material of Construction 16
2.5 Full-scale Grit Chamber Design Data 17
2.6 Pilot-scale Grit Chamber Design Data 18
2.7 Design Considerations and Limitations 21
2.8 Design Validation 22
2.8.1 Geometric Similitude 22
2.8.2 Kinematic Similitude 24
2.8.3 Dynamic Similitude 25
2.9 Conclusion 26

Chapter 3 Tracer Study on Pilot-scale Aerated Grit Chamber

3.1 Introduction 27
3.2 Background 27
3.2.1 Tracer Injection 28
3.2.2 Tracer Response Analysis 30
3.2.2.1 Axial Dispersion Model 31
3.2.2.2 Tanks-in-series Model 32
3.2.2.3 Point Analysis 33
3.3 Experimental Methods 33
3.4 Results and Discussion 35
3.4.1 Axial Dispersion Model 38
3.4.2 Tanks-in-series Model 39
3.4.3 Point Analysis 40
3.4.4 General Discussion 40
3.5 Conclusion 42

Chapter 4 Grit Sampling and Analysis
4.1 Introduction 43
4.2 Grit Characteristics 43
4.2.1 Physical Properties 44
4.2.2 Grit Classification 45
4.3 Collection of Samples 45
4.3.1 Effluent Sample Collection 45
4.3.2 Influent Sample Collection 47
4.3.3 Solid Grit Collection 47
4.4 Analytical Procedures 48
4.4.1 Total Suspended Solids (TSS) Analysis 48
4.4.2 Fixed Solids (FS) and Volatile Solids (VS) Analysis 50
4.4.4 Fixed Solids and Volatile Solids in Solid Grit Sample 51
4.4.5 Sieving Procedure 52
4.5 Results and Discussion 53
4.6 Conclusion 61

Chapter 5 Laser Measurements of Hydraulic Jet Mixing in Pilot-scale Mixing Tank
5.1 Introduction 62
5.2 Planar Laser Induced Fluorescence 63
5.2.1 Theoretical Background 64
5.2.2 PLIF and Hydraulic Jets 65
5.3 Experimental Equipments 66
5.3.1 PLIF Instrumentation 66
5.3.1.1 Fluorescent Dye 66
5.3.1.2 Laser Source 67
5.3.1.3 CCD Camera and Image Processing 68
5.3.2 Flow Equipments 68
5.3.2.1 Injectors and Nozzles 68
5.3.2.2 Pilot –scale Mixing Tank 69
5.4 Experimental Setup and Methodology 72
5.4.1 PLIF Calibration 72
5.4.2 Image Acquisition 72
5.4.3 Tracer study with KCl 74
5.5 Results and Discussion 74
5.6 Conclusion 85

Chapter 6 General Conclusions 86

References 88

Appendix A: Raw Data of Tracer Study on Pilot-scale Grit Chamber 92
Appendix B: Raw Data of Gravimetric Analysis of Liquid Grit Sample 93
Appendix C: Raw Data of Sieve Analysis of Solid Grit Sample 98
Appendix D: Stress Calculation for Pilot-scale Grit Chamber 100

LIST OF TABLES

Table 2.1: Results of design calculations for the full-scale grit chamber 17
Table 2.2: Results of design calculations for the full-scale grit chamber 19
Table 3.1: Definition of points used in point analysis of RTD 33
Table 3.2: Summary of experimental parameters in tracer study 34
Table 3.3: Summary of mean residence time and variance of RTD 37
Table 3.4: Point analysis of RTD of pilot-scale grit chamber 40
Table 4.1: Physical properties of grit 44
Table 4.2: Grit Classification 45
Table 4.3: Parameters for grit size distribution analysis 53
Table 4.4: Results of grading parameters for oven-dried grit and ignited grit 58
Table 4.5: Results of fixed solids content (%) for different sieve fraction 59
Table 4.6: Results of grit chamber influent analyses 60
Table 5.1: Summary of the operating parameters of jet experiments 73
Table 5.2: Operating conditions for PLIF instruments 74
Table 5.3: Mean and variance of tracer response with 4 opposing jets 84

LIST OF FIGURES

Figure 1.1: Flow diagram of wastewater treatment at Gold Bar WWTP 3
Figure 2.1: Spiral flow pattern in an aerated grit chamber 14
Figure 2.2: Layout of pilot-scale model of aerated grit chamber 18
Figure 2.3: The pilot-scale model of aerated grit chamber 20
Figure 3.1: KCl concentration vs. conductivity at 20^0C 35
Figure 3.2: RTDs for pilot-scale aerated grit chamber 35
Figure 3.3: RTD for pilot-scale grit chamber operating without aeration 37
Figure 3.4: Dimensionless RTD for pilot-scale aerated grit chamber 38
Figure 3.5: Comparison of tanks-in-series model and experimental tracer data 39
Figure 4.1: Effluent sampling site for aerated grit chamber #7 at Gold Bar WWTP 47
Figure 4.2: Variation in TSS in effluent along the depth in the grit chamber 54
Figure 4.3: Variation in FSS in effluent along the depth in the grit chamber 55
Figure 4.4: Variation in VSS in effluent along the depth in the grit chamber 55
Figure 4.5: Particle size distribution of grit particles 57
Figure 4.6: Grit particles retained on 4760 μm sieve 58
Figure 5.1: Mazzei injector (Model A-3) and Mazzei mixing nozzle 68
Figure 5.2: Layout of the mixing tank designed to facilitate various jet assemblies 70
Figure 5.3: PLIF Instruments 71
Figure 5.4: PLIF Experimental setup 71
Figure 5.5: PLIF images comparing two and four jets mixing 75
Figure 5.6: PLIF images comparing four and six jets mixing 76
Figure 5.7: PLIF images comparing six and eight jets mixing 77
Figure 5.8: PLIF images comparing opposing and alternating jets mixing 78
Figure 5.9: F-curve for mixing tank with 4 opposing jets (PLIF study) 81
Figure 5.10: F-curve for mixing tank with 4 opposing jets (KCl tracer study) 81
Figure 5.11: Change in dispersion number with number of jets 84

CHAPTER 1

INTRODUCTION

1.1 Problem Background

The critical task of designing any process equipment can be broken down into four basic steps (Joshi and Ranade, 2003): a) acquiring a complete knowledge of process requirements and identifying the desired flow dynamics characteristics; b) specifying possible reactor configurations and operating procedures to achieve the desired fluid dynamics characteristics; c) developing quantitative relationships between the reactor configuration and performance; and d) fine-tuning the final reactor design to achieve optimum conditions. In all four steps, the importance of knowledge on reactor hydrodynamics is evident to ensure efficient performance of the process equipment.

Several pieces of information are available in literature to define the design criteria of an aerated grit chamber (ASCE and FSIWA, 1959). However, many of these criteria are recommended based on years of operational experience and surveys on plants performances (Neighbor and Cooper, 1965). Besides, the multiphase flow regimes inside an aerated grit chamber make it even more difficult to develop quantitative relationships defining reactor parameters (such as physical properties, size distribution and velocity pattern of all three phases, tank geometry, operating flow rates and so on) and underlying physical processes (such as differential settling, scouring, mixing, solid breakage and so on). In order to investigate the design and operational issues pertaining to such complex flow phenomena, the most logical choice is to construct a scaled-down model to replicate flow conditions inside the full-scale unit.

This work aims at designing a pilot-scale model of the full-scale aerated grit chamber # 7 operating at Gold Bar wastewater treatment plant (WWTP). Experiments on the scaled-down model will invariably result in considerable savings in time, effort and money (Ettema, 2000). This work also explores the grit conditions of the full-scale grit chamber # 7 in an attempt to evaluate tank's performance. Finally, the thesis investigates the application of hydraulic jets in a pilot-scale mixing tank through laser measurement techniques.

1.2 Preliminary Treatment at Gold Bar Wastewater Treatment Plant

The Gold Bar wastewater treatment plant (WWTP) is a tertiary treatment plant located in the North Saskatchewan River valley in Edmonton, Alberta. The plant is designed to treat yearly approximately 95,000 ML of wastewater, including discharges from both sanitary and combined sewer systems. The treatment processes consists of grit separation, screening, primary settling, biological treatment in a suspended growth activated sludge system, secondary settling and UV disinfection. The primary treatment capacity of the plant was recently upgraded from 920 ML/day to 1600 ML/day by introducing an enhanced primary treatment unit to reduce combined sewer overflows during wet-weather conditions. Figure 1.1 shows the flow diagram of Gold Bar WWTP.

The preliminary treatment process at Gold Bar WWTP consists of removal of grit in aerated grit chambers and separation of large debris and solids from wastewater through mechanical bar screens. Wastewater arriving at Gold Bar flows directly into aerated grit chambers where denser particles are settled to the bottom of the tank via differential sedimentation and less dense particles remain suspended by aeration. After leaving the

grit chambers, the wastewater passes through mechanical bar screens with openings between 10 mm and 19 mm that prevents wood, rags, plastics and other large, heavy debris from entering the downstream treatment processes.

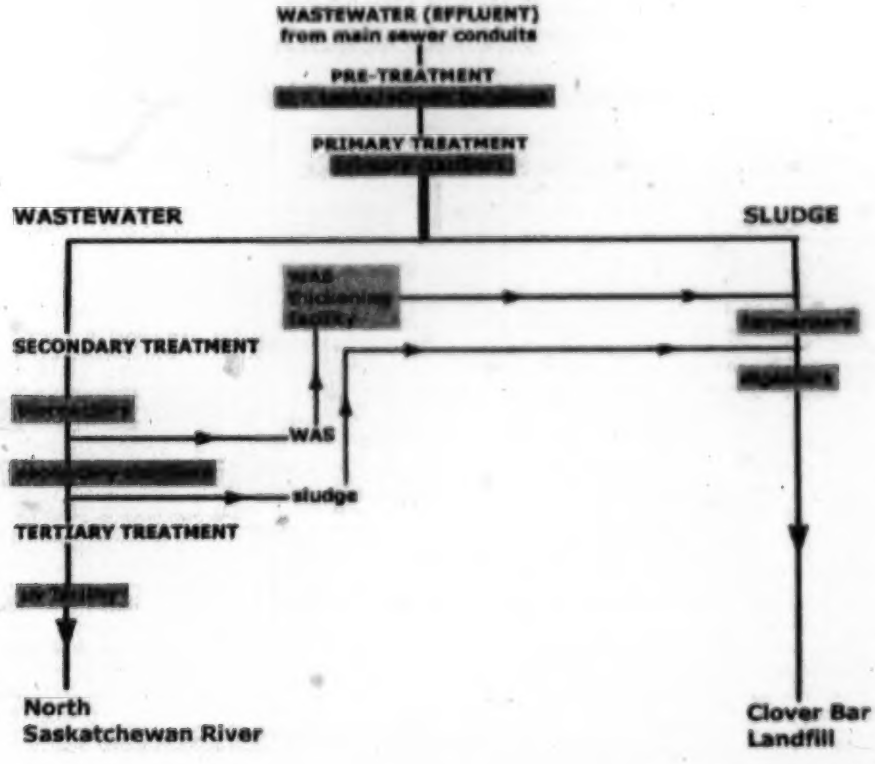

Figure 1.1 Flow diagram of wastewater treatment process at Gold Bar WWTP

The Gold Bar WWTP has seven aerated grit chambers and all of these are in operation during peak flow periods. Grit settled at the bottom of the grit chambers is collected either intermittently by clam shell buckets (installed in three older tanks), or continually by screw conveyors (in four newer tanks). The removed grit is dewatered either in an enclosed vortex chamber or by an inclined screw conveyor and is then transported to the Clover Bar landfill site.

1.3 Aerated Grit Chamber

An aerated grit chamber can be considered as a special type of settling tank designed for selective separation of grit larger than a desired size. Typical design guidelines recommend that a properly functioning aerated grit chamber should be capable of removing: a) 100% of coarse sand fraction (d> 0.2 mm) and 65-75% of the medium sand fraction (0.1<d<0.2 mm); b) organic content in the removed grit should be less than 10% by weight (Sawicki, 2004). The suggested geometric dimensions of the aerated grit chamber are as follows (WEF and ASCE, 1992):

- Depth = 2-5 m
- Length : Width ratio = 2.5:1 – 5:1
- Width: Depth ratio = 1:1 – 5:1 (typically 2:1)

The minimum detention time at peak hourly flow should be between 2-5 minutes, typically 3 minutes. Medium to coarse bubble diffusers are usually recommended for providing aeration in the grit chamber. Plant process air can be applied for aeration, however, dedicated blowers are recommended. The distance of aerators from the bottom of the tank should be between 0.6-1.0 m. The usual air flow rate range from 0.27-0.74 $m^3min^{-1}m^{-1}$ (4.6-12.4 L $s^{-1}m^{-1}$), 0.45 $m^3min^{-1}m^{-1}$ is the typical. Wider and /or deeper tanks require higher rate of aeration (WEF and ASCE, 1992).

Although a variety of grit removal devices (such as vortex-type grit chamber, horizontal-flow type grit chamber, detrius tank and hydrocyclone) are utilized in wastewater treatment, aerated grit chambers are favoured over others as they offer some important advantages, including: a) pre-aeration of sewage; b) minimal head loss; c) relatively low putrescible organic content in the settled grit; d) high flexibility and

adaptability to variable field conditions; e) the chamber can be used for chemical addition, mixing and flocculation prior to primary treatment (Albrecht, 1967). However, certain disadvantages are associated with aerated grit chambers, these include: a) high power consumption; b) additional labour and maintenance requirement for the aeration system; c) possible release of potentially harmful volatile organic compounds and odours from wastewater during aeration; d) lack of exact relationships defining the spiral flow within the chamber.

The indicators of poor performance of some full-scale aerated grit chambers are high organic content in the removed grit, low grit removal efficiency and abnormal grit loads in the grit collection system occurring periodically. Possible reasons for such problems could be (WEF and ASCE, 1992): a) poor design of tank geometry; b) incorrect placement of air diffusers; c) uncontrolled and unsteady rate of aeration and d) improper baffle position resulting in short circuiting and poor hydraulics control. From the above discussion it is evident that selective separation of grit larger than the desired size and with specific physical property requires close control over the tank hydraulics.

1.4 Scope of the Thesis

This thesis aims at (a) designing a pilot-scale model of an aerated grit chamber; (b) investigating the model hydrodynamics through tracer study; (c) analyzing grit conditions of the full-scale unit; and (d) exploring the application of hydraulic jet mixing through planar laser induced fluorescence (PLIF) study.

Chapter 2 describes the design and construction of the hydraulic model of the full-scale aerated grit chamber #7 at Gold Bar WWTP. The basic theory of similitude and

scaling relations derived from dimensionless numbers that are usually adopted for hydraulic modeling under various flow conditions are explained at the beginning of this chapter. This is followed by a detailed study on design and operation of the full-scale aerated grit chamber. The hydrodynamic conditions inside the tank were comprehended by consulting pertinent literature focusing on aerated grit chambers. All these investigations as well as selection of appropriate dynamic similitude criteria, scale factor and material of construction are discussed in section four of this chapter. Section five represents the design and operational specifications of the full-scale aerated grit chamber while section six represents the calculated geometric dimensions and operating parameters for the scaled-down model. The design limitations and subsequent modifications are discussed in section seven. The pilot-scale model design was validated through scaling ratios of dynamic similitude criteria which are presented in section eight. Finally a brief conclusion is provided at the end of the chapter.

Chapter 3 describes the findings of tracer study performed on the model aerated grit chamber. The chapter begins with a short introduction (section one) which is followed by a thorough discussion of theory behind tracer study, different tracer injection methods and various analytical procedures usually adopted in explaining the tracer response (section two). The experimental methodology followed during tracer study is stated in section three. The tracer responses were analyzed in three different procedures as found in literature and the results are explained in section four.

In an attempt to appreciate the performance of the full-scale aerated grit chamber, grit samples were collected from the tank's influent and effluent stream as well as from the grit hopper. The detailed description of sampling procedure and subsequent analyses

are provided in Chapter 4. The first two sections provide a review of relevant literature concentrating on grit properties and characteristics. Then the sample collection procedure is described in section three. The different analytical procedures employed for sample analyses are presented in section four. The results of grit sample analyses are illustrated in section five and a brief synopsis of the findings is provided in section six.

While designing the pilot-scale grit chamber, a mixing tank was built with provisions to incorporate jets in the tank. The mixing tank was designed to maintain identical width to depth ratio as that of the model grit chamber. The total hydraulic flow rates for both models were also designed to be identical. The mixing tank was specially designed to improvise jet mixing phenomena and to perform a baseline study to incorporate hydraulic jets in grit chamber operation. PLIF measurements were conducted to understand the mixing phenomena inside the tank. Chapter 5 describes the jet mixing study performed on this pilot-scale mixing tank through PLIF. In the first section of this chapter, pertinent literature is cited as a starting point for establishing the foundation for exploring hydraulic jets in grit chamber operation. Then a theoretical background of laser measurement technique and its application in jet mixing study is provided in section two. The laser instruments and flow equipment that were used in the study are illustrated in section three. Section four describes all the operating parameters for jet-mixing as well as methodology followed during PLIF image acquisition, calibration and tracer study. In section five, the images of PLIF measurements were presented and the data were further analyzed in an attempt to quantify the mixing effect of hydraulic jets. At the end, a summary of chapter findings is provided in section six. Chapter 6 presents the general conclusions of the findings of the thesis and recommendations for future studies.

CHAPTER 2

DESIGN OF PILOT-SCALE AERATED GRIT CHAMBER

2.1 Introduction

Physical modeling has been widely accepted as an important tool to investigate the design, operation and performance of any hydraulic system. This is also known as hydraulic modeling where a complex flow pattern or a specific physical process happening in a full-scale hydraulic system is replicated in a smaller scale (Ettema, 2000). In this study, the aerated grit chamber #7 at Gold Bar wastewater treatment plant (WWTP) was selected as the full-scale unit and a pilot-scale model was built based on similitude criteria.

2.2 Similitude

The principle of hydraulic modeling is based on similitude (Ettema, 2000). A model is said to have full similitude with its full-scale version when the following three conditions are met:

2.2.1 Geometric Similitude

Geometric similitude indicates that the ratios of all homologous linear dimensions are equal for the model and the full-scale unit, in other words, the model has the same shape as the full-scale system. Geometric similitude requires the length ratio L_R, to be constant for all parts of the model and the actual full-scale unit. L_R is defined as:

$$L_R = \frac{L_F}{L_M} \qquad (2.1)$$

where $_F$ and $_M$ refer to full-scale unit and the pilot-scale model, respectively.

2.2.2 Kinematic Similitude

Kinematic similitude indicates that ratios of velocities and accelerations at all homologous points in model and full-scale system are constant, in other words, the model has similar fluid streamline pattern as the actual unit. Kinematic similitude requires the velocity ratio U_R, to be constant at all homologous points of the model and full-scale unit. U_R is defined as:

$$U_R = \frac{U_F}{U_M} \qquad (2.2)$$

or $U_R = \frac{L_R}{T_R}$ (2.3) where time ratio, T_R is defined as $T_R = \frac{T_F}{T_M}$

where $_F$ and $_M$ refer to full-scale unit and the pilot-scale model, respectively.

2.2.3 Dynamic Similitude

Dynamic similitude indicates that the force polygons at all homologous points in the model and full-scale unit are similar and in the same ratio. Dynamic similitude requires the force ratio F_R, to be constant at all homologous points of the model and actual unit. F_R is defined as: $F_R = \frac{F_F}{F_M}$ (2.4)

where $_F$ and $_M$ refer to full-scale unit and the pilot-scale model, respectively. It is important to note that once the geometric and dynamic similitude is achieved between the model and prototype, the kinematic similitude is automatically satisfied.

2.3 Dynamic Similitude Criterion

One method of achieving the dynamic similitude between a model and the prototype is through equality of dimensionless parameters. Dimensionless parameters can be achieved by direct comparison of forces relevant to a hydrodynamic system. One such

dimensionless group is Froude number; Fr. Fr is expressed as the ratio of inertial force (F_i) to gravitational force (F_g) and leads to:

$$Fr^2 = \frac{F_i}{F_g} = \frac{\rho L^2 U^2}{\rho L^3 g} = \frac{U^2}{gL} \qquad (2.5)$$

$$\text{or, } Fr = \frac{U}{\sqrt{gL}} \qquad (2.6)$$

where ρ is the fluid density, L is the characteristic length, g is the gravitational acceleration and U is the fluid velocity. Another common dimensionless group used for achieving dynamic similitude is the Reynolds number, Re, which is expressed as the ratio of inertial force (F_i) and viscous force (F_v).

$$Re = \frac{\rho L^2 U^2}{\mu UL} = \frac{\rho LU}{\mu} \qquad (2.7)$$

where μ is the fluid viscosity. From the definitions of Froude number and Reynolds number, it becomes evident that each dimensionless group defines a unique relationship with scale ratio L_R, U_R and T_R. For example, if a model is built based on Froude number similitude criterion then the following relations can be deduced:

$$Fr_R = \frac{Fr_F}{Fr_M} = \frac{\left(U/\sqrt{gL}\right)_F}{\left(U/\sqrt{gL}\right)_M} = 1 \qquad (2.8)$$

If it is assumed that both the model and the full-scale unit are subjected to the same gravitational field then, $g_R = 1$ and the above relation becomes:

$$Fr_R = \frac{U_R}{\sqrt{L_R}} = 1 \qquad (2.9)$$

$$\text{or, } U_R = \sqrt{L_R} \qquad (2.10)$$

then, $T_R = \frac{L_R}{U_R} = \sqrt{L_R}$ (2.11)

If the same model is built based on the Reynolds number similitude criterion then the following relations can be obtained

$$Re_R = \frac{Re_F}{Re_M} = \frac{\left(\rho LU/\mu\right)_F}{\left(\rho LU/\mu\right)_M} = 1 \quad (2.12)$$

$$\text{or, } Re_R = \frac{U_R L_R}{\left(\rho/\mu\right)_R} = 1 \quad (2.13)$$

$$\text{therefore, } U_R = \frac{\nu_R}{L_R} \quad (2.14)$$

where ν (= μ/ρ) is the kinematic viscosity of the fluid:

$$\text{then, } T_R = \frac{L_R}{U_R} = L_R{}^2 \nu_R \quad (2.15)$$

From the above discussion it is clear that Froude number and Reynolds number each provide unique relations with scale ratios and these relations do not compliment each other. In other words, simultaneous satisfaction of both Froude and Reynolds number similitude are not achievable between the model and the full-scale system, unless the model fluid property is manipulated (Ettema, 2000). Therefore, it is very important to identify the forces dominating the system hydrodynamics.

The flow condition in a hydraulic structure can be influenced by several physical phenomena, such as inertia, gravity, buoyancy, drag, friction, pressure, surface tension and so on. It is also possible to produce several dimensionless parameters by regrouping the forces mentioned above and each of these dimensionless numbers can be used as a criterion for attaining dynamic similitude. For example, when scaling up or down a system, Froude number can be used for gravity-driven flow; Reynolds number can be

used for viscosity-dominating flow; Mach number is used for compressible flow; Weber number is used when surface tension is important. This indicates the fact that it is extremely important to recognize the controlling forces in a system and select the appropriate dimensionless group accordingly in order to simulate a specific process or flow phenomena in a model and maintain dynamic similarity simultaneously.

2.4 Pilot-scale Model Design Strategy

The first consideration in designing the pilot-scale model of the aerated grit chamber was to study the full-scale aerated grit chamber and gather all the necessary background information pertaining to design and operation of the system. The second step was to acquire a sound understanding of the underlying physical processes taking place in the grit chamber. This knowledge was then applied to select an appropriate similitude criterion to maintain dynamic similarity within the full-scale unit and the pilot scale model. This step was followed by completion of necessary calculations to define the geometric dimension and flow conditions for the pilot-scale model. The final step was to verify the pilot-scale design based on the similitude criterion and scaling relation.

2.4.1 Full-scale Aerated Grit Chamber at Gold Bar WWTP

The Gold Bar WWTP has seven aerated grit chambers for removing grit from wastewater. Of these seven tanks, grit chamber # 7 was selected as the full-scale model for this pilot-scale design study. This grit tank is 36.10 m long, 6.40 m wide 7.09 m deep. The cross sectional view of the chamber shows that the tank perimeter has the shape of a polygon. The tank has an inclined bottom sloping towards a hopper located near the right

hand side of the chamber. The right hand side wall of the tank is 4.10 m deep. After this depth, the wall slants inward at an angle of 48 degrees creating a 1.41 m deep slope. The left hand side wall of the tank is 3.58 m deep. After this depth, the wall makes a 0.91 m deep slope at 45 degrees and then again slopes inward at 7 degrees toward the hopper. The hopper is 0.63 m deep and 0.46 m wide and has a round bottom. An inclined screw conveyor system is installed at the bottom of the grit chamber that continually collects grit from the hopper. This conveyor pulls the settled grit out of the chamber and puts it into grit bins located at the head of the tank.

The grit chamber is equipped with coarse bubble diffusers located on the right hand corner of the tank (when looking from inlet end) and cover almost the entire length of the chamber. The diffusers are installed 1.64 m above the tank bottom. The hopper is placed beneath the air diffusers. The tank has a rectangular inlet gate, 1.83 m wide and 2.28 m long and is located at the bottom left corner of the tank. The outlet gate is also rectangular in shape, 1.80 m wide and 2.55 m long and is located at the upper right corner of the chamber. There is no baffle at inlet or outlet of the chamber. The maximum design capacity of this grit chamber is 300×10^3 m^3day^{-1}. The water column depth inside the tank is maintained at 5.79 m. The corresponding average detention time is 6.08 min under the above condition. The rate of aeration for this grit chamber varies from 0.37 – 0.65 m^3min^{-1} per unit length (m) of the tank.

2.4.2 Hydraulic Considerations of Full-scale Aerated Grit Chamber

The aerated grit chamber can be considered as a special type of settling tank equipped with an aeration system and designed for selective separation of grit (Sawicki,

2004). In grit chamber #7, air bubbles are introduced near the bottom of the grit chamber and perpendicular to the incoming wastewater. The combination of these two fluid flows creates a spiral roll flow pattern inside the tank where wastewater makes several passes depending on the flow rate (Tchobanoglous et al., 2003). During this rolling action, denser particles (usually the inert ones) drop to the bottom due their higher settling velocities. Less dense particles, mostly the organic portion of the grit remain suspended by the roll and eventually get carried away with the effluent. Finally, the settled particles at the tank bottom are driven into the grit hopper by the spiral flow of wastewater. Figure 2.1 shows operation of a typical grit chamber.

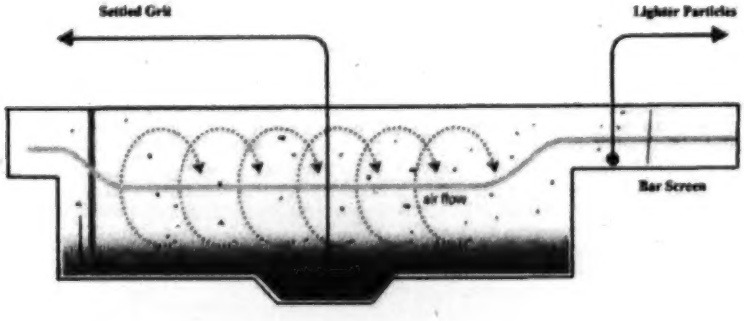

Figure 2.1 Spiral flow pattern in an aerated grit chamber

Settling of grit in aerated grit chambers depends on three main factors: size and specific gravity of the grit particles and the velocity of roll in the tank. Velocity of roll is governed by both the rate of air diffusion and tank geometry. Therefore, by adjusting the rate of air diffusion, it is possible to remove any specified size of grit with a given specific gravity. Besides, the rolling action is independent of wastewater flow through the tank. So the aerated grit chamber can efficiently operate over a wide range of flows without compromising the performance (WEF and ASCE, 1992).

The typical design criterion for aerated grit chamber is based upon removal of grit particles having specific gravity of 2.65 and the particles are considered to be mostly inorganic in nature. Grit is removed from wastewater via sedimentation and the sedimentation mechanism can be explained in terms of differential settling. This process states that particles with higher specific gravities (usually the inorganic ones) settle to the bottom due to their higher settling velocities. Any organic particles that settle to the bottom with the grit are subjected to bottom scour which reintroduces them into the main flow stream. It has been reported that to move grit particles of 0.20 mm size and specific gravity of 2.65 into the grit hopper, a flow velocity of approximately 0.23 ms^{-1} is required (ASCE and FSIWA, 1959). At 0.91 ms^{-1}, sand particles begin to move upward in the vertical direction (Neighbor and Cooper, 1965). In actual practice, most grit chambers operate at a flow velocity within 0.20 to 0.40 ms^{-1} (ASCE and FSIWA, 1959).

2.4.3 Dynamic Similitude Criterion

Froude number similitude criterion is the major principle commonly followed to design hydraulic models governed by gravitational forces such as free surface flows (Ettema, 2000). As mentioned earlier, aerated grit chambers are primarily designed to induce grit sedimentation, and since it is a free surface flow, therefore inertia and gravity are the predominant forces controlling the hydrodynamic condition in the grit chamber. That is why, Froude number similitude criterion needs to be maintained in designing the pilot-scale grit tank and to preserve dynamic similitude between the model and the full-scale unit. The Froude number similitude criterion is expressed as,

$$Fr_R = \frac{Fr_F}{Fr_M} = \frac{\left(U/\sqrt{gL}\right)_F}{\left(U/\sqrt{gL}\right)_M} = 1 \qquad (2.16)$$

where $_F$ and $_M$ refer to full-scale unit and the pilot-scale model, respectively.

2.4.4 Scale Factor

All the geometric dimensions of the full-scale grit chamber were scaled down using a scale factor of 15. Several factors were considered while selecting the scale factor. First of all, the model's horizontal scale needed to be chosen in such a way so as to fit the limited floor space. Secondly, the constraint of maximum hydraulic flow rate attainable under the existing laboratory facility was also considered. And finally, material and construction costs were considered while selecting the scale factor.

2.4.5 Material of Construction

The model grit chamber was built with clear acrylic plastic, also known as PMMA (polymethyl-methacrylate). This material was selected due to its optically transparent nature and high strength to weight ratio. Besides, acrylic can be easily bended and machined without much difficulty thus enabling construction of critical geometric shapes with greater accuracy. The solvent bonding property of acrylic also produces strong but invisible seam lines. The model grit chamber was constructed with 1.91 cm (¾ inch) thickness of acrylic sheet. This thickness was chosen based on flexural stress calculation. The average flexural yield strength for acrylic is 99.2 MPa (www.matweb.com) and was higher than the calculated stresses exerted by water column on tank walls (Appendix D).

2.5 Full-scale Grit Chamber Design Data

The first step of hydraulic model design was to investigate the design and operation of the existing full-scale grit chamber. For this purpose, engineering drawings of the grit chamber were thoroughly studied and relevant geometric dimensions were extracted. Site visits were also made to find out about grit chamber's operating conditions such as tank's peak flow rate, aeration rate, water column depth, type and placement of aerators inside the tank. Based on those investigations, the following parameters were calculated as shown in Table 2.1.

Table 2.1: Results of design calculations for the full-scale grit chamber

Parameter	Units	Full-scale unit values
Length	mm	36100
Width	mm	6401
Water column depth	mm	5794
Hopper length	mm	36100
Hopper depth	mm	858
Hopper bottom diameter	mm	458
Tank inlet area	m^2	4.18
Tank outlet area	m^2	4.59
Hydraulic flow rate	m^3s^{-1}	3.47
Tank inlet velocity	ms^{-1}	0.83
Tank outlet velocity	ms^{-1}	0.76
Average velocity inside the tank	ms^{-1}	93.62×10^{-3}
Hopper area	m^2	26.17
Hopper volume	m^3	4.33
Total inside area	m^2	61.20
Tank volume	m^3	1.27×10^3
Average detention time	sec	365
Air flow rate	m^3s^{-1}	13.36
Diffuser distance from tank bottom	mm	1640
Froude number at tank inlet		0.11
Froude number calculated from average velocity inside the tank	-	0.012
Reynolds number	-	540×10^3

2.6 Pilot-scale Grit Chamber Design Data

As mentioned earlier, the pilot scale model was built on 1/15th scale ratio. Figure 2.2 shows the engineering drawings of the scaled-down model.

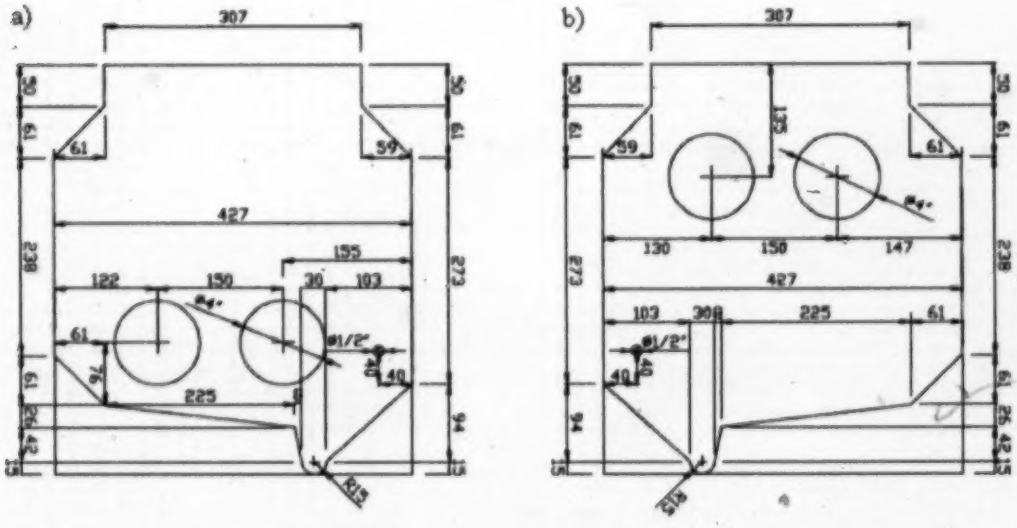

Figure 2.1 Layout of pilot-scale model of aerated grit chamber #7 at Gold Bar WWTP:

a) view of inlet wall; b) view of outlet wall (all dimensions are in mm)

The actual physical model is shown in Figure 2.3. Based on a flow capacity of 3.47 $\times 10^{-3}$ $m^3 s^{-1}$, inlet-outlet condition and some other operating parameters were calculated for the model. The results are shown in Table 2.2.

Table 2.2: Results of design calculations for the pilot-scale grit chamber

Parameter	Units	Pilot-scale model values
Length	mm	2401
Width	mm	427
Water column depth	mm	386
Hopper length	mm	2401
Hopper depth	mm	57
Hopper bottom diameter	mm	15
Tank inlet area	m^2	16.21×10^{-3}
Tank outlet area	m^2	16.21×10^{-3}
Hydraulic flow rate	m^3s^{-1}	3.47×10^{-3}
Tank inlet velocity	ms^{-1}	0.21
Tank outlet velocity	ms^{-1}	0.21
Average velocity inside the tank	ms^{-1}	21.05×10^{-3}
Hopper area	m^2	11.43×10^{-2}
Hopper volume	m^3	1.05×10^{-3}
Total inside area	m^2	269.84×10^{-3}
Tank volume	m^3	37.56×10^{-2}
Avg. detention time	sec	108
Air flow rate	m^3s^{-1}	2.56×10^{-4}
Diffuser distance from tank bottom	mm	109
Froude number at tank inlet		0.11
Froude number calculated from average velocity inside the tank	-	0.011
Reynolds number	-	8.09×10^{3}

a)

b)

Figure 2.3 The pilot-scale model grit chamber a) Set-up of the model

b) Transparent acrylic wall facilitating visual observation of flow condition.

2.7 Design Considerations and Limitations

While scaling down the geometric dimensions of the full-scale grit chamber, all dimensions were calculated in meters and rounded to 4 significant digits. This introduced some degree of round-off error; however, this step was necessary in order to make the dimensions meaningful to the craftsmen.

As mentioned earlier, the inlet and outlet gate of the full-scale grit chamber are rectangular in shape. However, it was not possible to incorporate such rectangular gates in the model, as rectangular piping and plumbing fittings are not commercially available. Instead, circular inlet and outlet were designed for this model and the corresponding diameters were chosen to maintain geometric similarity of full-scale and model inlet and outlet areas (at the 15:1 length scale). Nevertheless, there was another practical constraint that had to be considered while designing the inlet / outlet. There is a maximum size limit of commercially available circular pipes and fittings. The largest circular pipe fitting that was available at the time of model construction had a diameter of 10.16 cm. Therefore, to match the value of required inlet area (18.57×10^{-3} m^2); the only rational choice left was to design two circular inlets (as well as outlets) for this model. This gave a total inlet (or outlet) area of 16.21×10^{-3} m^2.

According to the Froude number similitude, the peak flow in the pilot scale chamber should be of 3.98×10^{-3} $m^3 s^{-1}$ corresponding to 300×10^3 m^3/day flow in full-scale grit chamber. Allowing this flow rate through the designed inlet area (16.21×10^{-3} m^2) would result in an inlet velocity of 0.25 ms^{-1}. This high velocity at the tank inlet would likely induce a higher velocity inside the tank as well. As mentioned earlier, due to size and shape constraint in piping and plumbing fittings, it was not possible to increase

the inlet flow area. For this reason, the hydraulic flow rate in the pilot scale grit chamber was maintained from 3.46×10^{-3} m^3s^{-1} to 3.52×10^{-3} m^3s^{-1} during tracer study (chapter 3). This arrangement was also reasonable due to the fact that full-scale aerated grit chambers are designed based on peak flow condition. This allows the grit chambers to handle variable flow conditions without compromising their performance (ASCE and FSIWA, 1959).

2.8 Design Validation

The successful design of any pilot-scale model depends on establishing geometric, kinematic and dynamic similitude with the full-scale unit. In this study, the pilot-scale model was designed so as to meet the Froude number similitude criterion. In this section the validation of model design is explained based on the scaling ratios derived from this similitude principle. As before, the scale factor is denoted as L_R and has a value of 15. The model and full-scale values are denoted as subscripts $_M$ and $_F$, respectively.

2.8.1 Geometric Similitude

- According to Froude number similitude criterion:

Length scale: $$L_R = \frac{L_F}{L_M} \qquad (2.17)$$

Area scale: $$A_R = \frac{(L_F)^2}{(L_M)^2} = L_R{}^2 \qquad (2.18)$$

Volume scale: $$V_R = \frac{(L_F)^3}{(L_M)^3} = L_R{}^3 \qquad (2.19)$$

To check geometric similarity between the model and the full-scale unit, several dimensions such as length, width, water column depth; hopper length, width and bottom

diameter were compared between the full-scale unit and the scaled down model. Finally, tank inside area, inlet and outlet area, volume; hopper area and volume were compared and related to the scaling ratios mentioned above.

$$\text{Tank length ratio} = \frac{36100\text{mm}}{2407\text{mm}} = 14.99 \approx L_R$$

$$\text{Tank width ratio} = \frac{6401\text{mm}}{427\text{mm}} = 14.99 \approx L_R$$

$$\text{Water column depth ratio} = \frac{5794\text{mm}}{386\text{mm}} = 15.01 \approx L_R$$

$$\text{Hopper length ratio} = \frac{36100\text{mm}}{2407\text{mm}} = 14.99 \approx L_R$$

$$\text{Hopper depth ratio} = \frac{858\text{mm}}{57\text{mm}} = 15.05 \approx L_R$$

$$\text{Hopper bottom diameter ratio} = \frac{458\text{mm}}{30\text{mm}} = 15.27 > L_R$$

$$\text{Tank inlet area ratio} = \frac{4.18\text{m}^2}{16.21\times10^{-3}\text{m}^2} = (16.06)^2 > L_R^2$$

$$\text{Tank outlet area ratio} = \frac{4.59\text{m}^2}{16.21\times10^{-3}\text{m}^2} = (16.82)^2 > L_R^2$$

$$\text{Tank inside area ratio} = \frac{61.20\text{m}^2}{269.84\times10^{-3}\text{m}^2} = (15.05)^2 \approx L_R^2$$

$$\text{Hopper area ratio} = \frac{26.17\text{m}^2}{114.30\times10^{-3}\text{m}^2} = (15.13)^2 \approx L_R^2$$

$$\text{Tank volume ratio} = \frac{1.27\times10^{3}\text{m}^3}{375.63\times10^{-3}\text{m}^2} = (15)^3 = L_R^3$$

$$\text{Hopper volume ratio} = \frac{4.33\text{m}^3}{1.05\times10^{-3}\text{m}^2} = (16)^3 > L_R^3$$

Discrepancies were observed when the tank inlet, outlet and hopper area ratios were compared with the similitude scaling ratios. The differences in inlet-outlet areas between the pilot scale model and the full-scale system were due to the practical limitations of pipe fittings as mentioned earlier. The discrepancy in hopper area was due to rounding-off error introduced while designing the diameter of the hopper bottom.

2.8.2 Kinematic Similitude

According to Froude number similitude criterion:

$$\text{Velocity scale: } U_R = \frac{\sqrt{L_F}}{\sqrt{L_M}} = L_R^{0.5} \qquad (2.20)$$

$$\text{Time scale: } T_R = \frac{\left(L/U\right)_F}{\left(L/U\right)_M} = \frac{\sqrt{L_F}}{\sqrt{L_M}} = L_R^{0.5} \qquad (2.21)$$

$$\text{Flow rate scale: } Q_R = \frac{\left(UL^2\right)_F}{\left(UL^2\right)_M} = U_R \times L_R^{\,2} = L_R^{0.5} \times L_R^{\,2} = L_R^{2.5} \qquad (2.22)$$

To check dynamic similarity between the model and the full-scale unit, ratios of wastewater and air flow rate; inlet, outlet and average velocity were calculated and compared to the scaling ratios mentioned above. The average hydraulic detention time were compared with time scaling ratio as well.

$$\text{Tank hydraulic flow rate ratio} = \frac{3.47 m^3 s^{-1}}{3.47 \times 10^{-3} m^3 s^{-1}} = (15.85)^{2.5} > L_R^{2.5}$$

$$\text{Tank aeration rate ratio} = \frac{13.42 m^3\ min^{-1}}{15 \times 10^{-3} m^3\ min^{-1}} = (15.15)^{2.5} \approx L_R^{2.5}$$

$$\text{Tank inlet velocity ratio} = \frac{0.83 ms^{-1}}{0.21 ms^{-1}} = (15.08)^{0.5} \approx L_R^{0.5}$$

$$\text{Tank outlet velocity ratio} = \frac{0.76 ms^{-1}}{0.21 ms^{-1}} = (12.50)^{0.5} < L_R^{0.5}$$

$$\text{Tank average inside velocity ratio} = \frac{93.62\times10^{-3}\,\text{ms}^{-1}}{21.05\times10^{-3}\,\text{ms}^{-1}} = (19.77)^{0.5} > L_R{}^{0.5}$$

$$\text{Average detention time ratio} = \frac{365\text{s}}{108\text{s}} = (11.42)^{0.5} < L_R{}^{0.5}$$

The discrepancy in average inside velocity arose when the pilot scale model was operated at lower hydraulic flow rate to compensate the smaller inlet flow area. This also explains the disagreement between actual and theoretical time scale ratios. However, it can be argued that the discrepancy in average flow velocity is merely an approximation. This is due to the fact that velocity inside an aerated grit chamber is practically controlled by the rate of air diffusion (ASCE and FSIWA, 1959). This makes the rate of aeration an important parameter influencing the flow condition inside grit chamber. For this study, the rate of aeration (2.50×10^{-4} m^3s^{-1}) was close to desired value (2.56×10^{-4} m^3s^{-1}) which indicated that the model was operating within acceptable flow condition.

2.8.3 Dynamic Similitude

According to the Froude number similitude criterion, dynamic similarity is established between a model and a full-scale system when

$$Fr_R = \frac{Fr_F}{Fr_M} = 1 \qquad (2.23)$$

To check kinematic similarity between the model and the full-scale unit, ratios of Froude number at inlet and outlet were calculated and compared to the scaling ratios mentioned above.

$$\text{Ratio of Froude number at tank inlet} = \frac{110.25\times10^{-3}}{109.97\times10^{-3}} = 1.00 = Fr_R$$

$$\text{Ratio of Froude number at tank outlet} = \frac{100.34\times10^{-3}}{109.97\times10^{-3}} = 0.91 < Fr_R$$

Ratio of Froude number inside tank = $\frac{12.42\times10^{-3}}{10.82\times10^{-3}} = 1.14 > Fr_R$

The above discussion indicates that the pilot-scale design of aerated grit chamber follows the Froude number similitude criterion quite satisfactorily. This proves that all three similitude prerequisites were successfully maintained while scaling down the full-scale unit and therefore, the model will be able to replicate the full-scale flow pattern adequately.

2.9 Conclusion

In this study, a pilot-scale model was built, replicating the full-scale aerated grit chamber # 7 at Gold Bar WWTP. The full-scale unit was scaled down by 1/15th scale factor. The flow inside the grit chamber was considered to be dominated by gravity and inertia. Therefore, Froude number similitude criterion was selected to establish dynamic similarity between the model and full-scale unit and to validate the model design in terms of geometric, kinematic and dynamic similitude. It was necessary to make some modifications of tank's inlet and outlet configuration due to some practical limitations of pipe fittings. The operating conditions were fine-tuned accordingly. The model was validated based on Froude number similitude criterion and scaling ratios which showed that all three similitude prerequisites were maintained satisfactorily between the model and the full-scale grit chamber unit.

CHAPTER 3

TRACER STUDY ON PILOT-SCALE AERATED GRIT CHAMBER

3.1 Introduction

Determination of residence time distribution (RTD) by tracer study has been proven to be a powerful tool in characterization of fluid flow in various types of chemical reactors (Kulkarni et al., 2007), biological reactors in wastewater treatment (Olivet et al., 2005), underground reservoirs and water distribution systems (DiGiano et al., 2005). Tracer studies provide valuable insight in flow pattern and mixing phenomena which in turn helps in assessing reactor performance and optimizing process parameters (Smith et al., 1993). In this work, tracer studies were carried out on the pilot-scale grit chamber and RTD curves were generated to have a better knowledge of tank hydrodynamics. The tracer responses were further scrutinized by various analytical methods to characterize the flow condition inside the vessel.

3.2 Background

Fluid flow phenomena in a vessel under steady-state condition can be categorized into two idealized reactor models (Levenspiel, 1996). One is continuous stirred tank reactor (CSTR), where the inlet flow is perfectly and instantly mixed into the bulk fluid and fluid composition is homogenous everywhere inside the tank and identical with outlet. The other one is plug flow reactor (PFR), in which the flow is perfectly mixed in the radial direction but there is no mixing in the axial direction. Flow inside the PFR can be reflected as a series of plugs traveling in the axial direction, each with a uniform composition but different from the ones before and after it. In other words, an infinite

number of CSTRs connected in series approximates the PFR condition. In practical situation most fluid vessels operate somewhere between these two extremes.

Residence time distribution (RTD) is a measure of the amount of time fluid elements spend inside a reactor. This is one of the important factors utilized for characterizing flow and mixing in reactors. Analysis of RTD provides a measure of real reactor's deviation from ideal flow condition as well as prediction about presence of dead zones, channeling or short-circuiting within the flow field (Olivet et al., 2005). RTD is often referred to as the E-curve where E(t) has the dimension of time^{-1} and defined as

$$\int_0^\infty E(t)dt = 1 \qquad (3.1)$$

3.2.1 Tracer Injection

Experimental determination of RTD involves tracer study where a tracer material is introduced into the fluid stream entering the reactor and the concentration is measured in the fluid stream leaving the system. The tracer is usually non-reactive in nature and is introduced into the fluid stream without upsetting the hydrodynamic condition of the reactor. The two most common methods utilized for introducing tracer are pulse input and step input. Two other methods for tracer injection are periodic and random input where tracer is injected in the inlet with varying concentration either in periodic and random manner. However the latter two methods of tracer injection require more rigorous calculation for RTD curve interpretation.

In pulse input, a small volume of tracer is injected into the inlet stream in a very short time interval so that it approaches a Dirac delta function. In this case, the E-curve is given by:

$$E(t) = \frac{QC(t)}{M} \tag{3.2}$$

where Q is the volumetric flow rate through the reactor, C(t) is the tracer concentration in effluent at time t and M = mass of tracer injected. Assuming 100% recovery of tracer in the outlet, a mass balance on tracer gives (Robinson and Tester, 1986):

$$\frac{M}{Q} = \int_0^\infty C(t)dt \tag{3.3}$$

Combining Eqs. (3.2) and (3.3) gives

$$E(t) = \frac{C(t)}{\int_0^\infty C(t)dt} \tag{3.4}$$

This relation is utilized to normalize experimental data recorded from pulse tracer study and to construct RTD curves. The mean residence time $\bar{t}$, and variance σ^2, for the E(t) function can be calculated as:

$$\bar{t} = \frac{\int_0^\infty tC(t)dt}{\int_0^\infty C(t)dt} \tag{3.5}$$

$$\sigma^2 = \frac{\int_0^\infty t^2C(t)dt}{\int_0^\infty C(t)dt} - (\bar{t})^2 \tag{3.6}$$

In step input, tracer is injected in a steady state to approach a step function. In this case, tracer concentration at the inlet abruptly changes from 0 to C_0. The tracer concentration measured at the outlet of the reactor is normalized with C_0 to obtain a dimensionless function F(t) where:

$$F(t) = \frac{C(t)}{C_0} \qquad (3.7)$$

The normalized curve is known as F-curve which goes from 0 to 1. The function F(t) and E(t) are related by the following

$$F(t) = \int_0^t E(t)dt \qquad (3.8) \qquad \text{and} \qquad E(t) = \frac{dF(t)}{dt} \qquad (3.9)$$

The choice of tracer input method is often governed by the ease of operation. However, step response often tends to smooth over some of the details in flow condition that pulse response can reveal quite distinctively. Pulse response can be easily integrated to obtain a very precise estimate of step response. However, the reverse is not the case as direct differentiation of experimental step response results in the amplification of any noise arising from analytical methods and concentration measurements (Martin, 2000).

An ideal CSTR, shows an exponential distribution of residence time given by:

$$E(t) = \frac{1}{\tau} e^{-\frac{t}{\tau}} \qquad (3.10)$$

whereas an ideal PFR gives a delta distribution of residence time as following:

$$E(t) = \delta(t - \tau) \qquad (3.11)$$

where τ is the theoretical hydraulic residence time (calculated as $\tau = V/Q$ where V is the reactor volume and Q is the volumetric flow rate through the reactor) (Nauman, 2004).

3.2.2 Tracer Response Analysis

Several models have been proposed to explain flow behaviour of real vessels and their deviations from two ideal extremes (CSTR and PFR) based on RTD analysis. Commonly quoted models are described below.

3.2.2.1 Axial Dispersion Model

This model is based on the ideal plug flow with a diffusive component superimposed in the axial direction. The concept is based on applying Fick's law in the longitudinal direction at steady state condition which gives the following relation

$$D_L \frac{\partial^2 C(t)}{\partial x^2} = u \frac{\partial^2 C(t)}{\partial x} + \frac{\partial C(t)}{\partial t} \qquad (3.12)$$

where D_L is the longitudinal dispersion coefficient, C(t) is the concentration at time t, u is the fluid velocity and x is the length in axial direction (Levenspiel, 1996). When concentration, time and length are converted to dimensionless parameters C(= C (t) / C_0), θ (= t / $\bar{t}$) and z (= x/L, L is the length of the reactor) then the above equation becomes:

$$\left(\frac{D_L}{uL}\right)\frac{\partial^2 C}{\partial z^2} = \frac{\partial C}{\partial z} + \frac{\partial C}{\partial \theta} \qquad (3.13)$$

The magnitude of dispersion is quantified by the dimensionless dispersion number N_D:

$$N_D = \frac{D_L}{uL} = \frac{1}{Pe} \qquad (3.14)$$

where Pe is the Peclet number. The analytical expressions for dispersion model is not available in Levenspiel (1996) but stated elsewhere (Martin, 2000). However, expressions for the mean and variance of the dispersion model are mentioned by Levenspiel (1996) for different boundary conditions.

For a non-ideal E-curve, the dispersion model is highly influenced by the boundary conditions of the reactor. Closed boundary conditions apply to the reactor when the fluid stream enters and leaves the reactor in idealized plug flow but changes to disperse flow within the reactor (Martin, 2000). In this case, the dispersion number is calculated as:

$$\sigma_\theta^2 = \frac{\sigma^2}{(\bar{t})^2} = 2\frac{D_L}{uL} - 2\left(\frac{D_L}{uL}\right)^2\left(1 - e^{-uL/D_L}\right) \qquad (3.15)$$

For an ideal plug flow N_D is 0 (Pe = ∞) and goes to ∞ (Pe = 0) for an ideal CSTR.

3.2.2.2 Tanks-in-series Model

In this model flow through a reactor is characterized by a series of N equal-volume hypothetical CSTRs. There are several ways to predicts values for N. One method is to calculate N from the variance of the RTD curve as following:

$$N = \sigma^2 / (\bar{t})^2 \qquad (3.16)$$

Another method is to construct RTD curves for various N and compare them with experimentally obtained RTD curves. The general relations utilized here are:

$$\theta = t / (\bar{t}) \qquad (3.17)$$

$$E(\theta) = \frac{N(N\theta)^{N-1}}{(N-1)!} e^{-N\theta} \qquad (3.18)$$

The number of tanks, N, characterizes the dispersion with N = 1 representing infinite dispersion in an ideal CSTR while a reactor with ideal plug flow will have infinite number of tanks in series.

Tanks-in series model is much easier to handle than the axial dispersion model. Also the precise definition of boundary conditions is not required for this model (Levenspiel, 1996). However, one drawback of this model is that N has to be integer while many real CSTRs lies between N = 1 to 2 (Martin, 2000).

3.2.2.3 Point Analysis

Another method of RTD analysis is to examine the curve at various points as shown in Table 3.1. However, point analysis of RTD curve often leads to confusing and inconsistent results (Smith et al., 1993) and therefore, is not applied commonly.

Table 3.1 Definition of points used in point analysis (Smith et al., 1993)

Point	Definition
t_{10}	time for 10% of tracer to exit reactor
t_{90}	time for 90% of tracer to exit reactor
t_p	time to reach maximum tracer concentration
t_g	time to reach centroid of the curve
t_h	time for 50% of tracer to exit reactor
t_{90}/t_{10}	Morrill Index of mixing
$1-t_p/t_g$	Index of short-circuiting

Besides these, several other models have been proposed in literature to analyse RTD in unsteady state (Fernandez-Sempere et al., 1995), in recycle system (Battaglia et al., 1993) and internal RTDs in maldistributed flow (Robinson and Tester, 1986).

3.3 Experimental Methods

Tracer studies were carried out (in replicates) on the pilot-scale grit chamber under two different set ups, with and without aeration, respectively. A solution of 1.87 M potassium chloride (KCl) was used as the tracer in these experiments. The grit chamber had two feed lines with same dimensions and geometry. Therefore, equal amounts of tracer were injected simultaneously into the two influent lines just before the tank inlets

and the injection time was kept as short as possible to approach pulse tracer input. A summary of the experimental conditions for tracer study is shown in Table 3.2.

Table 3.2 Summary of experimental parameters in tracer study

Parameters	Tracer study			
	1	2	1	2
Tank volume (m^3)	37.56×10^{-2}	37.56×10^{-2}	37.56×10^{-2}	37.56×10^{-2}
Hydraulic flow rate (m^3s^{-1})	3.50×10^{-3}	3.47×10^{-3}	3.46×10^{-3}	3.52×10^{-3}
Average hydraulic residence time (s)	107	108	109	106
Aeration rate (m^3s^{-1})	-	-	2.60×10^{-4}	2.60×10^{-4}
Tracer (KCl) concentration (M)	1.87	1.87	1.87	1.87
Tracer volume (ml)	40	30	35	35

Tracer concentration was monitored continuously at the tank outlet using a conductance-resistance meter (YSI Model 34) and dip conductivity cell (YSI 3417). Calibration of the conductivity meter and the conductivity cell was carried out before the tracer experiment and necessary adjustments for temperature corrections were made to the conductivity values. The conductivity values were converted to concentration using the calibration curve shown Figure 3.1. Data collection spanned about twice the period of theoretical residence time. The time scales on these recordings were adjusted by subtracting the lag time for the tracer to reach tank inlet from point of injection. The raw data for tracer study are tabulated in Appendix A.

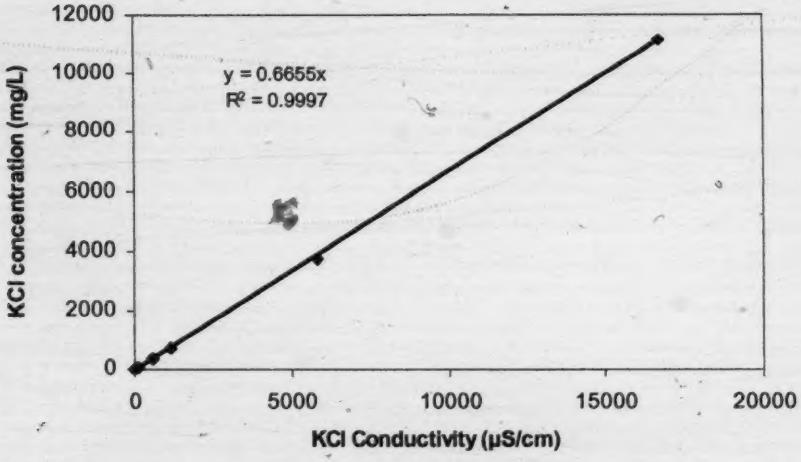

Figure 3.1 KCl concentration vs. conductivity at 20^0C

3.4 Results and Discussion

Tracer responses of the pilot-scale grit chamber operated with aeration are shown in Figure 3.2.

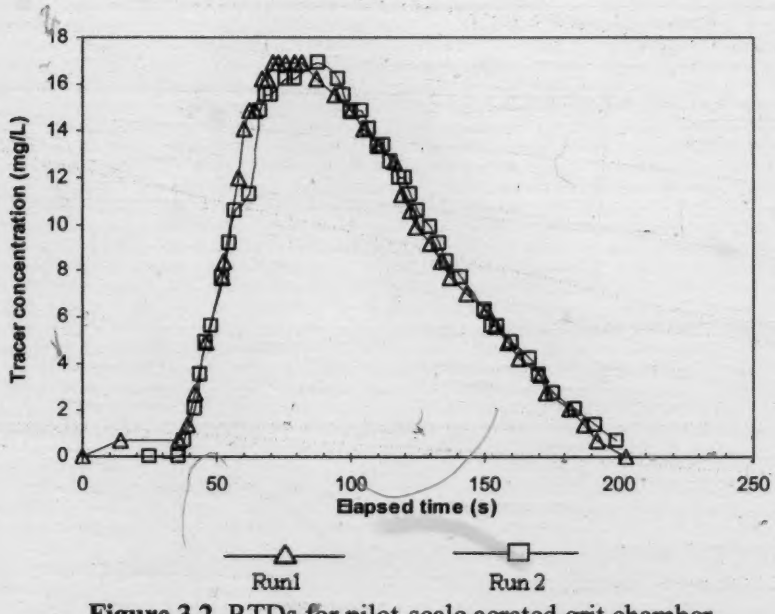

Figure 3.2 RTDs for pilot-scale aerated grit chamber

As seen in the above Figure, the RTDs for the grit chamber demonstrated reasonable reproducibility in replicate runs. The general trend of the RTDs showed a time lag of approximately 35 to 40 seconds before tracer can be detected at the tank outlet. The time lag was followed by a sharp increase in concentration to approach the peak (approximately 17 mgL^{-1} KCl) and finally a slow decrease in concentration to the initial level. A mass balance of tracer was carried out to check the consistency of the experiments which indicated the entire amount of tracer injected at the inlet was recorded at the tank outlet.

Another set of tracer analysis was performed on the pilot-scale grit chamber without any aeration. This was done to get a comparative image of RTD with and without aeration. Morales and Reinhart (1984) reported similar tracer dispersion patterns while conducting tracer experiments on a full-scale grit chamber operating with and without aeration. In this case, tracer response varied a lot for this pilot-scale grit chamber when operated under these two conditions. Figure 3.3 shows an example of RTD for non-aerated grit chamber. This curve had a noticeably different shape than that in Figure 3.2. The non-aerated RTD revealed some short peaks indicating possible channelling or short-circuiting in the fluid flow. The mean and variance of tracer pulse response were calculated by Eqs. 3.19 and 3.20 as stated in Levenspiel (1996). A summary of mean residence time and variance calculated from experimental RTDs for the runs mentioned in Table 3.2 is presented in Table 3.3.

$$\bar{t} = \frac{\sum_{i=1}^{n-1}(t_{i+1} + t_i)(C_{i+1} + C_i)(t_{i+1} - t_i)}{2\sum_{i=1}^{n-1}(C_{i+1} + C_i)(t_{i+1} + t_i)} \qquad (3.19)$$

$$\sigma^2 = \frac{\sum_{i=1}^{n-1}(t_{i+1}+t_i)^2(C_{i+1}+C_i)(t_{i+1}-t_i)}{4\sum_{i=1}^{n-1}(C_{i+1}+C_i)(t_{i+1}-t_i)} - \bar{t}^2 \qquad (3.20)$$

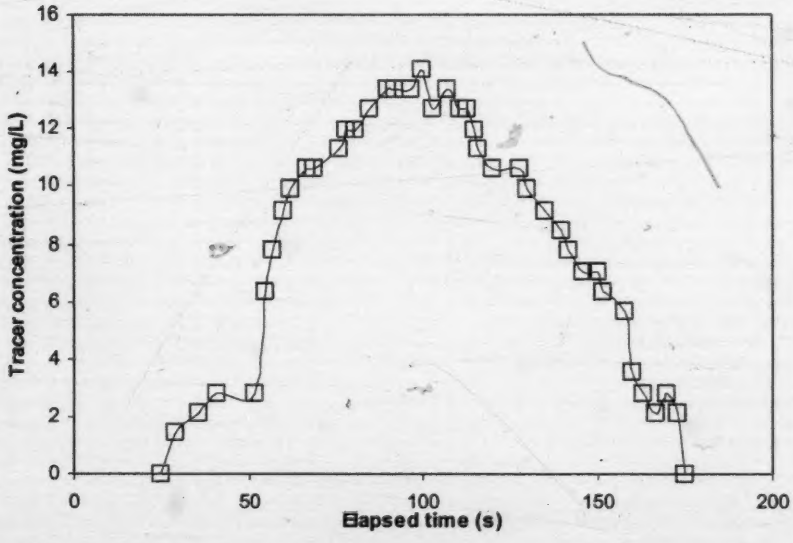

Figure 3.3 RTD for pilot-scale grit chamber operating without aeration (Run 2)

Table 3.3 Summary of mean residence time and variance of RTD

Parameter	Tracer Study			
	Without aeration		With aeration	
	Run 1	Run 2	Run 1	Run 2
Mean residence time (s)	98	102	103	99
Variance (s^2)	841	1020	1179	1231

It was evident form Figure 3.2 that the flow in the pilot-scale grit chamber could not be described as an ideal CSTR or PFR flow pattern. The observed RTDs always gave slightly shorter mean residence time than theoretical residence time (τ). This can be explained by the presence of dead zones accounted by the volume occupied by coarse bubble aerators. The non-zero variance pointed out dispersion along the tank length. In

fact, some degree of dispersion was not unexpected in the flow pattern of the pilot-scale grit chamber. The tank geometry and the aeration system operating perpendicular to hydraulic flow created a spiral clock-wise rolling action which was visually observed. All these may be attributed to create some degree of non-uniformity in tank velocity and/or turbulence. Therefore, it was necessary to apply a non-ideal model (tanks-in-series model, axial dispersion model etc.) to fit the experimental tracer data.

3.4.1 Axial Dispersion Model

As mentioned earlier, the analytical expression for axial dispersion model is not available in Levenspiel (1996). The dispersion number N_D was calculated from the dimensionless variance of the RTD curve (Eqn. 3.15) under closed boundary condition. Once the variance σ_θ^2 was found from the dimensionless RTD plot (shown in Figure 3.4), the dispersion number was calculated in iterative method using Excel 97® Solver tool pack. N_D was found to be 5.95×10^{-2} (Pe = 16.91) which indicated high degree of dispersion (Levenspiel, 1996). The value of dispersion coefficient, D was $3\times10^{-3}m^2s^{-1}$.

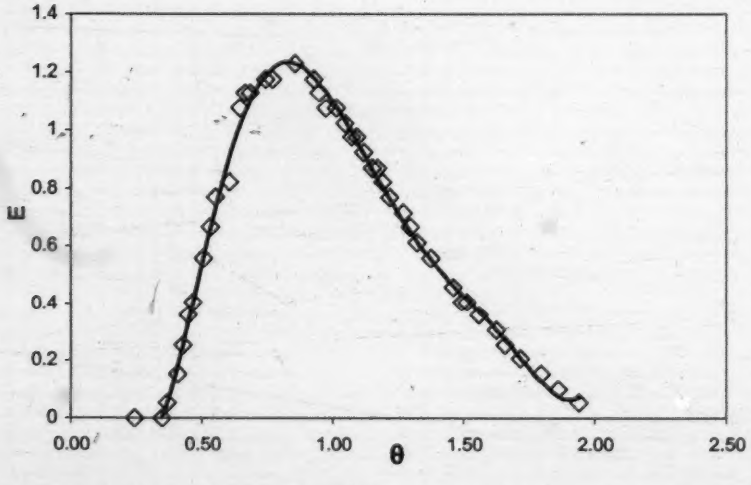

Figure 3.4 Dimensionless RTD for pilot-scale aerated grit chamber

3.4.2 Tanks-in series Model

Based on the Eqns. (3.17) and (3.18), several models were constructed by varying the number of tanks N. Best fit was found with nine ideal CSTRs in series, shown in Figure 3.5. It was observed that the normalized experimental tracer response matched quite successfully with the tanks-in series model. The only deviations were that the model slightly over-rated the peak concentration and approached the peak a little slower. Apart from these, the model was quite successful in predicting the flow pattern in the-pilot scale grit chamber. The maximum number of tanks-in-series was also calculated from the variance of the RTD curve by Eqn. (3.16) and gave consistent result (N = 9).

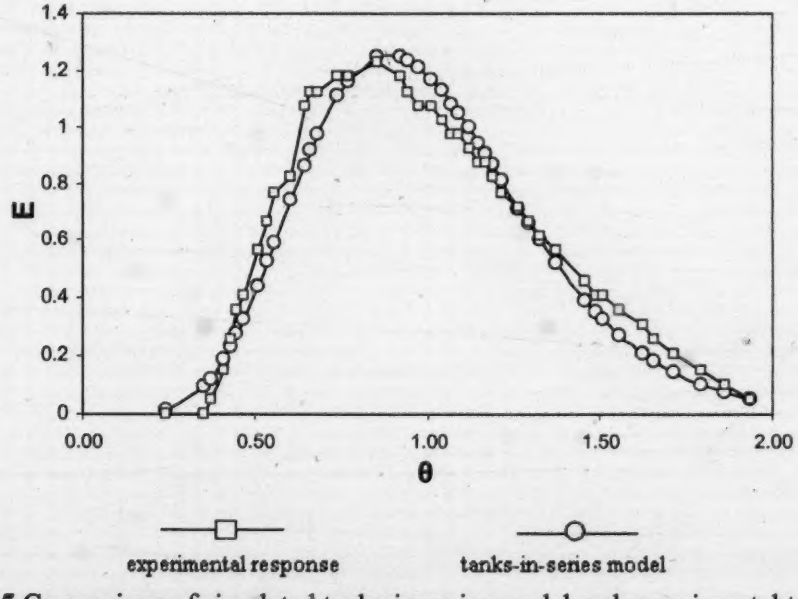

Figure 3.5 Comparison of simulated tanks-in-series model and experimental tracer data for pilot scale-aerated grit chamber

3.4.3 Point Analysis

The results of point analysis of tracer responses are presented in Table 3.4. Definitions of these points are provided in Table 3.1. The points were calculated from the RTD curves found in the experimental runs listed in Table 3.2.

Table 3.4 Point analysis of RTD of pilot-scale grit chamber

Points	Tracer study			
	Without aeration		With aeration	
	Run 1	Run 2	Run 1	Run 2
t_{10} (s)	62	62	59	56
t_{90} (s)	136	146	150	150
t_p (s)	92	100	88	80
t_g (s)	98	102	103	99
t_h (s)	94	99	96	93
t_{90}/t_{10}	2.19	2.35	2.54	2.68
$1-t_p/t_g$	0.06	0.02	0.15	0.2

Higher t_p values were observed when the grit chamber was operated without aeration. This indicated a reduced degree of mixing in the non-aerated grit chamber. However, the Morrill Index of mixing (t_{90}/t_{10}) was lower for non-aerated chamber which referred to better mixing phenomena and thus, contradicted the previous finding. This kind of mutual inconsistency between the point indices made the results of point analysis inconclusive and inadequate for describing flow pattern in the vessel.

3.4.4 General Discussion

The point analysis of tracer response is based on single values of the RTD curve. Martin (2000) suggested that this kind of analysis is only reliable when the tracer response is symmetrical and close to plug flow. In spite of its ease of use, point analysis

could not be considered dependable for the pilot-scale grit chamber due to the mutually inconclusive point indices.

The axial dispersion method is designed to fit best where the flow pattern being studied is close to plug flow. A disadvantage of this model is the lack of analytical expression. Nonetheless, accurate evaluation dispersion number is possible from the mean and variance of the RTD by defining the boundary conditions of the system properly. Literature is available stating the dispersion coefficients for a range of wastewater treatment units such as primary clarifiers, activated sludge clarifiers and aerated lagoons (Tchobanoglous, 2003); though no such published data were found for aerated grit chambers. Therefore, it was not possible to compare the dispersion number obtained in this study with published data.

The tanks-in-series model also works best with systems closer to plug flow and is simpler to handle than the axial dispersion model as it does not require exact definition of the boundary conditions. For small deviation from plug flow, the two models (axial dispersion and tanks-in-series) can be correlated as $1/N = 2\ (D_L/uL)$. However, for this pilot-scale grit chamber this relation was not in exact agreement for the two models. The value of N was 9 for tanks-in series model analogous to a dispersion number of 5.56×10^{-2}. The value of dispersion number calculated from the mean and variance of experimental RTD was 5.95×10^{-2}. Nonetheless, both these numbers proved that the flow pattern in the pilot-scale aerated grit chamber was subjected to high axial dispersion. Presence of some degree of back mixing and/or channelling was not unexpected inside the model, as the geometry of grit chamber and aerators location add together to create a spiral rolling flow of wastewater inside the tank.

The experimental RTD for the pilot-scale aerated grit chamber was best described with the model of nine CSTRs in-series. The proposed model captured the actual response quite remarkably as shown in Figure 3.5. Estimation of number of tanks obtained from the dimensionless variance of experimental RTD also verified the tanks-in-series model.

3.5 Conclusion

In this study, the flow pattern in the pilot-scale grit chamber was investigated by tracer experiments while operating the model with and without aeration. The tracer response was studied by applying two analytical methods, axial dispersion model and tanks-in-series model. Point analysis of the experimental RTD was also carried out. The results of point analyses were mutually inconclusive and insufficient for describing flow pattern in the model grit chamber. The axial-dispersion analysis reported a dimensionless dispersion number of 5.95×10^{-2} which indicated high degree of dispersion inside the tank. The non-ideal flow pattern for this model aerated grit chamber was best simulated by nine tanks-in-series model.

CHAPTER 4

GRIT SAMPLING AND ANALYSIS

4.1 Background

Aerated grit chambers are traditionally designed to achieve a complete removal of inorganic particles larger than 0.20 mm - 0.25 mm (Neighbor and Cooper, 1965). Although no single standard procedure exists for the evaluation of performance and efficiency of operating grit chambers, literature suggested a number of methods that had been undertaken. Morales and Reinhart (1984) determined grit removal efficiency by comparing grit deposits in the grit chamber with primary clarifier sludge. Finger and Parrick (1980) analyzed the discharges from grit dewatering units to assess the performance of grit chamber. Chasick and Burger (1964) tested the efficiency of grit chamber by judging the influent and effluent conditions. This method was also utilized by Albrecht (1967). Neighbor and Cooper (1965) employed the particle size distribution of grit chamber effluent as a basis for quantitative appraisal of removal efficiency.

In this study, an attempt has been made to evaluate the performance and grit condition in the aerated grit chamber #7 at Gold Bar WWTP. Samples were collected around this particular grit chamber to account for the grit entering, leaving and being removed by the system. These samples were further analyzed to obtain a better insight about the grit characteristics.

4.2 Grit Characteristics

Grit is a general term applied to the small and dense particles in the raw sewage which are predominantly inorganic in nature and commonly consist of sand, gravel, silt,

cinder, broken glass, metallic particles and other inorganic solids (Liu and Liptâak, 2000). Ideally grit is considered to have two basic characteristics: (a) grit should mostly contain inert material with little or no putrescible organic matter and (b) the settling velocities of grit particles should be considerably greater than those of putrescible organic matter. In reality, grit composition can be highly heterogeneous and often contains organic matter such as egg shells, seeds, coffee grounds, cigarette filter tips and similar other materials (Neighbor and Cooper, 1965; Liu and Liptâak, 2000).

4.2.1 Physical Properties

Several pieces of information are available in various literature describing the physical properties and composition of grit. Nonetheless, this information often differs from one another to some extent. This variability in properties arises from the heterogeneous nature of grit. Table 4.1 shows the physical properties of grit as stated in literature.

Table 4.1 Physical properties of grit

Grit Property	Range
Specific gravity	1.3 to 2.7; typically 2.65 [a,b]
Bulk density, (kgm^{-3})	1600 [b]
Moisture content (%)	13 to 65 [b]
Solid content (%)	35 to 80 [c]
Putrescible content (%)	Less than 3; up to 50 [a,b]
Size range (mm)	Above 0.20 to 0.25 [d]

[a] ASCE and FSIWA (1959)
[b] Tchobanoglous et al., (2003)
[c] WEF and ASCE (1992)
[d] Neighbor and Cooper (1965)

4.2.2 Grit Classification

Neighbor and Cooper (1965) classified grit into three main categories based on organic content and particle size distribution. The classification is shown in Table 4.2.

Table 4.2 Grit Classification

Characteristics	Class 1 grit	Class 2 grit	Class 3 grit
Grit condition	Clean and dry	Slightly odorous	Sloppy and highly odorous
Size of finer particles	No particle is finer than 250μm	A considerable amount is finer than 250μm	Particles finer than 149 μm are present
Putrescible organic content	None	Less than 0.7%	Extremely high
Volatile solid content	Extremely low	Less than raw sludge feed to digester	Same as the raw sludge feed to digester

4.3 Collection of Samples

For this study, wastewater samples were collected from the influent channel and near the effluent gate of the grit tank. Effluent samples were collected at different depths of the water column. Moreover, solid grit samples were collected from one of the grit bins. All of this sampling (effluent, influent and solid grit) was carried out on June 18, 2008 at the Gold Bar WWTP. A detailed description of sample collection procedure is presented in the following sections.

4.3.1 Effluent Sample Collection

Aerated grit chambers are expected to show spatial variation in composition of wastewater in the vertical direction. To capture this change in composition along the tank depth, grab samples were collected near the tank outlet approximately 3.50 m (11.5 ft)

below the top water surface and at about 0.15 m (0.5 ft) intervals. At each depth samples were collected in 500 ml wide-mouth plastic bottles (made from polytetrafluoroethylene) and each sampling was done manually over a short time period of 30-45 sec. A total of 24 samples were collected at 24 different depths in this experiment.

A sampling tool was specially designed to collect samples from aerated grit chamber. This tool consisted of a 1.22 m long graduated metal pole with a metal base at the end where sampling bottle was securely positioned. A side bar of equal length was attached parallel to the pole and the bar was connected to a bottle stopper fitting the 500-ml sampling bottle. This side bar was manipulated to pull open the bottle stopper once the bottle reached the desired depth. The sampling tool was extended up to 3.66 m by connecting two more metal poles and side bars.

The sampling location was situated just near the effluent gate of the grit chamber #7. Sample collection was a challenge itself as no sampling ports were available to collect effluent from the grit chamber. The effluent from grit chamber # 7 goes directly into a mechanical bar screen through a common channel and there was no provision to collect samples before the bar screen due to space limitation as well as safety considerations. Therefore, the only choice left was to collect samples from the tank as close to the outlet as possible to gain a representation the effluent condition. Figure 4.1 shows the location where effluent samples were collected.

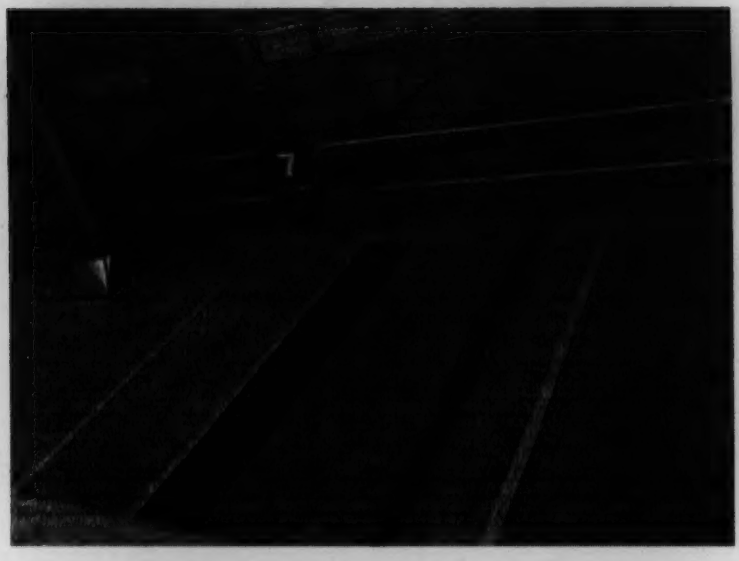

Figure 4.1 Effluent sampling site for aerated grit chamber #7 at Gold Bar WWTP

4.3.2 Influent Sample Collection

Grab samples from influent were collected from a combined channel feeding grit chambers # 4-7. Samples were collected in triplicates in 1-L wide-mouth sampling bottles made from fluorinated polymer. The sampling tools utilized to collect samples from the deep channel were similar to those used for effluent sampling. This time, samples were collected about 0.60 m below the top water surface in the channel.

4.3.3 Solid Grit Collection

Solid grit samples were collected from a pile of grit with a shovel. Samples were collected in small quantities at random fashion covering as many locations of the pile as were accessible. These multiple grab samples were combined together to approach to the same grading as the large pile. A total of 5 kg solid grit sample was collected in an air-tight plastic bucket.

All the samples (effluent, influent and solid grit) were transported back to the university laboratory on the same day. Cooler boxes packed with ice were used to store samples while transporting them back to the university. All samples were stored in the dark at 4^0C in a temperature-controlled room to minimize the potential for biodegradation before further analysis. However, samples were restored back to room temperature before any analysis was carried out.

4.4 Analytical Procedures

The following analyses were carried out on the influent and effluent wastewater samples: total suspended solids (TSS), fixed suspended solids (FSS), volatile suspended solids (VSS). The solid grit sample was investigated for particle size distribution by carrying out sieve analysis. Solids analysis and sieving were chosen because these were the only two methods invariably employed in literature for investigating grit chamber performance (Chasick and Burger, 1965; Neighbor and Cooper, 1965; Finger and Parrick, 1980).

4.4.1 Total Suspended Solids (TSS) Analysis

The term total suspended solids (TSS) refers to the dry-weight of the portion of solids retained by a filter of specific pore size and dried at a specific temperature. The following paragraphs describe the procedures followed for TSS determination based on Section 2540 D of Standard Methods (1999).

First, a glass-fiber filter disk (Pall Corporation, Type A/E) of 1 μm nominal pore size was placed in a Gooch crucible and washed with 20 ml deionized water in a vacuum manifold. This filter-crucible combination was oven dried at 103^0-105^0 C for 1h, ignited

in muffle furnace at 550^0C for 15 min, cooled in the desiccator, weighed on an analytical balance (Denver Instrument, Model APX 200) and the data was recorded as the initial weight, W_{iTSS}. The crucible was again placed on the vacuum manifold and the filter was wetted with deionized water to seat against the crucible.

Before any analysis, the collected sample was thoroughly mixed in order to achieve a uniform particle distribution. Then a pre-determined volume (30 to 50 ml) of sample was carefully poured into a graduated cylinder and filtered through the crucible placed in the vacuum manifold. The filter was rinsed with three successive 10 ml. portion of deionized water. The vacuum suction was allowed to continue until no traces of moisture were present. Finally the crucible was oven dried at 103^0-105^0 C for 2h, cooled in the desiccators, weighed on the analytical balance and the weight was recorded. The drying, cooling and weighing sequences were repeated until the change in the weight remained within 4%. The final dry-weight was recorded as W_{fTSS} and the TSS was calculated from the following relation:

$$TSS(mgL^{-1}) = \frac{W_{iTSS}(mg) - W_{fTSS}(mg)}{Volume_{sample}(L)} \qquad (4.1)$$

The above procedure was followed for the 48 effluent samples and the effluent sample.

For quality assurance and quality control (QA/QC) purpose, de-ionized water was tested for TSS as reagent blank. The blank TSS value was always found smaller than the samples' TSS value. Duplicate measurements of each sample were taken and the duplicates agreed within ± 0.5 % of their average weight. The difference between the duplicate sets was tested using student's t-test and it was shown to be non-significant ($t = 0.005$, p-value = 0.01 at 95% confidence level).

4.4.2 Fixed Solids (FS) and Volatile Solids (VS) Analysis

Fixed solids (FS) refers to the solid residuals left from suspended solids after heating to dryness at a specified temperature over a specified time. The weight lost at ignition is called volatile solids (VS) (Standard Methods, 1999).The FS and VS were measured according to Section 2540 E of Standard Methods (1999) and the procedure is described below.

The residues obtained from TSS analysis were ignited to constant weight in a pre-heated muffle furnace at a temperature of 550^0C. After ignition, the crucibles were partially cooled in open air to dissipate some heat and subsequently transferred to desiccator for final cooling. The crucibles were weight on an analytical balance as soon as the temperature balanced. These igniting, cooling, desiccating and weighing sequences were repeated until the change in the weight remained within 4%. The final weights for the TSS samples were recorded as W_{550TSS}. The FS and VS for theses samples were found as the following:

$$FSS(mgL^{-1}) = \frac{W_{550TSS}(mg) - W_{iTSS}(mg)}{Volume_{sample}(L)} \qquad (4.2)$$

$$VSS(mgL^{-1}) = \frac{W_{fTSS}(mg) - W_{550TSS}(mg)}{Volume_{sample}(L)} \qquad (4.3)$$

where FSS and VSS represents fixed and volatile solid portions, respectively, of TSS.

For QA/QC purpose, a blank glass fibre filter was ignited at 550^0C along with other samples to check the applicability of the filter. It was proven positive as no appreciable weight loss was observed. All measurements were taken in duplicates and the duplicates agreed within ± 0.5 % of their average weight.

4.4.4 Fixed Solids and Volatile Solids in Solid Grit Sample

Fixed solids (FS) and volatile solids (VS) in solid grit samples were analyzed according to Section 2540 G of Standard Methods (1999) in the following manner.

First, a pre-washed Gooch crucible was oven dried at 103^0-105^0 C for 1h, ignited in a muffle furnace at 550^0C for 15 min, cooled in the desiccator, and weighed on an analytical balance which was recorded as the crucible weight, W_C. Then a predetermined amount of sample (ranging from 25 to 40 gm) was transferred into the crucible and dried in an oven at 103^0-105^0 C for 2 h. When the sample was dry, the crucible was put in the desiccator to balance temperature and weighed subsequently. The drying, cooling and weighing sequences were repeated until the change in the weight remained within 4%. The final dry-weight was recorded as W_{105^0C}. The dried residue was ignited in a muffle furnace at 550^0C for 1 h. After ignition, the crucibles were partially cooled in open air to dissipate some heat and subsequently transferred to desiccator for final cooling. The crucibles were weighed on an analytical balance as soon as the temperature balanced. These igniting, cooling, desiccating and weighing sequences were repeated until the change in the weight remained within 4%. The final weight was recorded as W_{550^0C}. The fixed solids and volatile solids were calculated using the following relation –

$$FS(\%) = \frac{W_{550^0C}(gm) - W_C(gm)}{W_{105^0C}(gm) - W_C(gm)} \qquad (4.4)$$

$$VS(\%) = \frac{W_{105^0C}(gm) - W_{550^0C}(gm)}{W_{105^0C}(gm) - W_C(gm)} \qquad (4.5)$$

In each case duplicate measurements were taken and the values were within ± 1% of their average weight. The raw data of above mentioned gravimetric analyses on grit samples are presented in Appendix B.

4.4.5 Sieving Procedure

The sieve analysis of solid grit sample was carried out based on the procedures described by Head (1980). A predetermined amount of grit (1.22kg) was weighed on a balance and placed on a pre-weighed aluminium tray. The sample was allowed to dry overnight, in an oven at 105^0C. After drying to constant weight, the sample was cooled and weighed and recorded as the initial dry-weight, m_i.

The sample was then washed on a 4760μm sieve nested over a 74μm sieve. A small portion of sample was placed at a time on the 4.7 mm sieve and washed over a sink with a spray of clean water. When the sample on the 4.7 mm sieve was washed free of fines, washing on 74μm sieve was continued until the water passing through the sieve ran clear. Care was taken not to overload the sieves. For this reason, the whole sample was divided into several portions and each was washed separately.

After completing the washing step, the whole of the material retained on each sieve was carefully transferred to the pre-weighed aluminium tray and dried overnight on an oven at 105^0C. The dried sample was then cooled, weighed and the data was recorded as dry-weight after washing, m_w. The finer particles lost by washing was then calculated form the difference between m_i and m_w.

Next, the sample was passed through a nest of sieves covering the size range of 4760μm down to 74μm. A set of 8 sieves of A.S.T.M. E-11 specification (USA standard) were used. The sieve sizes were 4760, 200, 850, 594, 420, 210, 150 and 74μm. The whole nest of sieves along with the sample was securely fastened on a portable sieve shaker (Combustion Engineering, Model RX-T792) and the sample was agitated for 10 minutes. Finally, the portion retained on each sieve was weighed and recorded.

Another set of sieve analysis was carried out on the solid grit with some modifications in the above procedure. For this set, a pre-weighed amount (1.29kg) of solid grit was dried overnight at 105^0C, cooled, weighed and then ignited at 550^0C in a muffle furnace. After ignition the sample was cooled and weighted. This was followed by subsequent washing on a 4760μm sieve nested over a 74μm sieve; drying at 105^0C, cooling, weighing and finally sieving through 4760, 200, 850, 594, 420, 210, 150 and 74 μm sieves. This method of igniting grit sample at 550^0C before sieving was suggested by Finger and Parrick (1980) in their grit size distribution study. The results of sieve analysis for these two procedures were compared based on the following parameters shown in Table 4.3. The raw data of sieve analyses are presented in Appendix C.

Table 4.3 Parameters for grit size distribution analysis

Parameter	Definition
D_{10}	size for which 10% of particles are finer
D_{30}	size for which 30% of particles are finer
D_{60}	size for which 60% of particles are finer
$C_u(= D_{60}/D_{10})$	Coefficient of uniformity
$C_c[= D_{30}^2/(D_{10}\times D_{60})]$	Coefficient of curvature

4.5 Results and Discussion

The working principle of any aerated grit chamber is based on differential settling of grit particles which is influenced by size and specific gravity of the particles as well as the spiral velocity in the tank. Difference in grit composition is expected along the vertical direction of the grit chamber as heavier particles settle to the bottom and lighter organic particles remain suspended in the tank. In order to get a quantitative appraisal of such variation, grit samples were collected at different depths of the water column near

the tank effluent and solid analyses were carried out on those samples. Figures 4.2 to 4.5 represent the result of these analyses on grit chamber effluent.

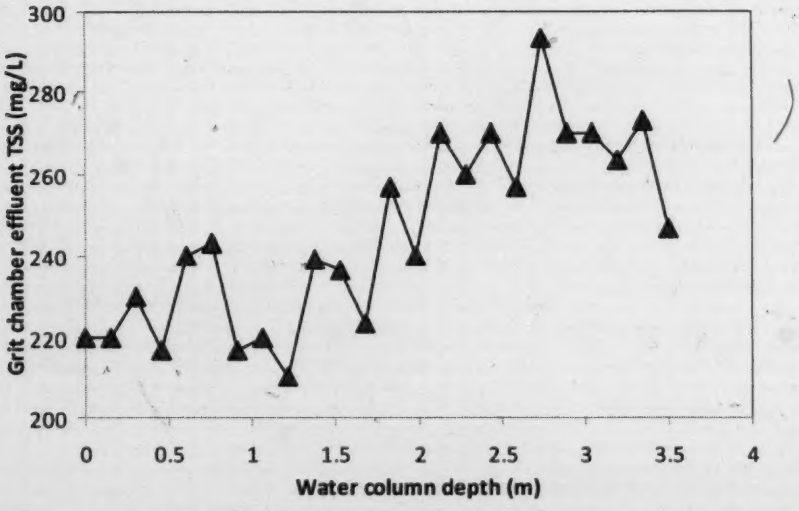

Figure 4.2 Variation in TSS concentration in effluent along the depth in the grit chamber

Figure 4.2 shows the depth-wise TSS variation of the grit chamber effluent. The curve showed a random TSS pattern with increasing depth up to 1.22 m where the lowest TSS (210 mgL^{-1}) was found at 1.37 m. This random pattern was followed by an overall increase in TSS (with fluctuations at regular interval along the depth) with the increase in depth. This rising trend of TSS continued up to 2.90 m where the highest concentration (293 mgL^{-1}) was observed. This peak was followed by a rapid decrease in TSS which continued until the final depth (3.5 m) was reached.

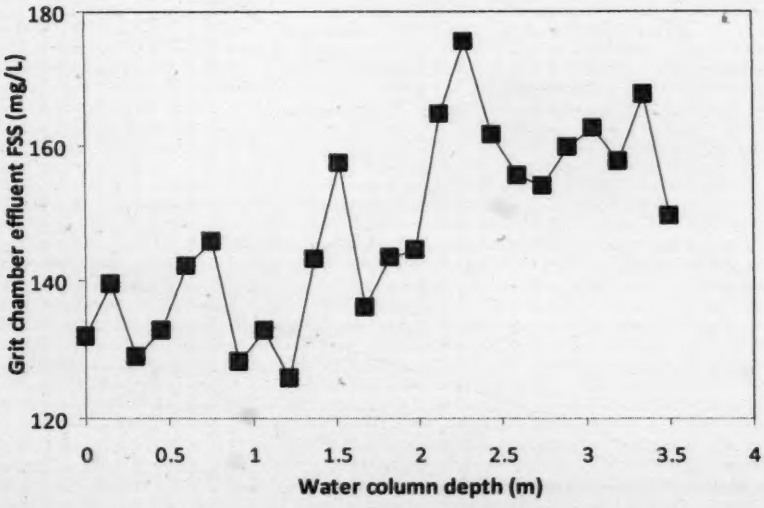

Figure 4.3 Variation in FSS concentration in effluent along the depth in the grit chamber

Figure 4.3 shows the fixed suspended solids (FSS) concentration variation along the tank depth. No particular trend was noticed in this data set as well. The maximum FSS (176 mgL^{-1}) was found at 2.29 m and the minimum FSS (126 mgL^{-1}) was found at 1.22 m. Figure 4.4 shows the depth-wise volatile suspended solid (VSS) variation of the grit chamber effluent. Again no particular trend was observed in this data set.

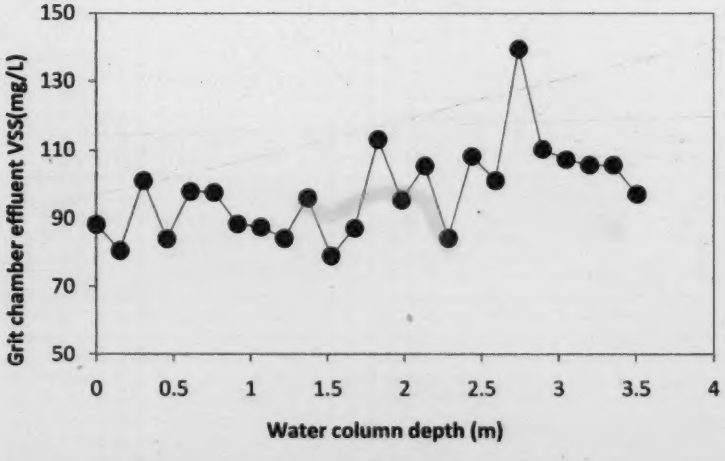

Figure 4.4 Variation in FSS concentration in effluent along the depth in the grit chamber

Initial observation of solid grit samples collected from the grit bin indicated a possible class 3 type of grit. The grit was mostly cohesive in nature and possessed an offensive odour pointing towards a possible high content of putrescible organic matter. Total solid (TS) analysis indicated the samples to be 42.46% dry solids by weight which in turn indicated moisture content greater than 50% in the raw grit sample. The fixed solid (FS) measurement showed 60.75% by weight of TS was FS (volatile solid (VS) content of 39.25%). The FS and VS content can be considered as a rough estimate of the inorganic and organic content of the sample, respectively. Nevertheless, VS may include some portion of mineral salts volatilized during the ignition, therefore, the exact amount of inorganic or organic content cannot be found from this analysis.

The solid grit consisted of a mixture of particles varying in a wide range of sizes and shapes. To classify these particles into separate sizes and to determine their relative proportions it was necessary to perform a sieve analysis. Sieving is a procedure to categorize samples consisting mostly of gravel and sand. It is predominantly applied to particles ranging from approximately 60 mm to 60 μm (Head, 1980).

As the grit sample contained a substantial amount of silt and clay, considered as finer particles, a wet sieving procedure was carried out in order to determine the proportion of the fine solids. In the wet sieving procedure, a sample was washed in water before sieving to ensure complete separation of fine particles. The finer particles were allowed to run to waste and the retained material was then dry sieved. The portion of finer particles was calculated from the difference between the unwashed and washed masses after drying.

Prior to sieving, a grit sample can be prepared by two separate procedures as suggested in literature. Both of these procedures were tested in this experiment. In the first procedure, the raw grit sample was dried at 105^0C and then wet-sieved (Head, 1980). In the second procedure, the raw grit sample was dried at 105^0C and then ignited at 550^0C before wet-sieving was carried out (Finger and Parrick, 1980). The results sieve analysis for these two procedures are shown in Figure 4.5.

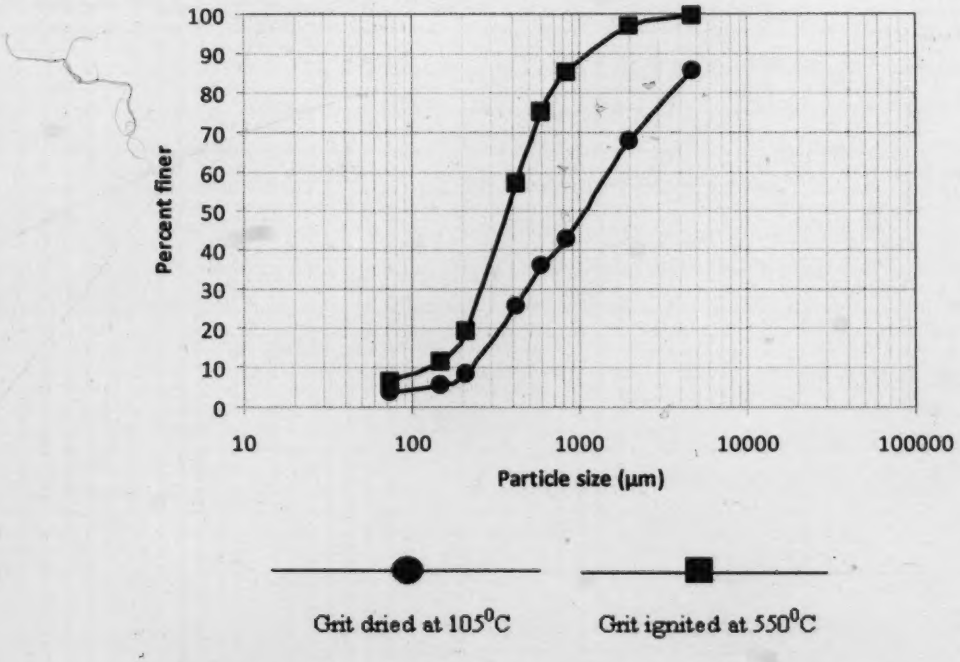

Figure 4.5 Particle size distribution of solid grit through sieve analysis

The particle size distribution (PSD) curves were constructed by plotting percentages finer than any given size against the sieve openings in a semi-logarithmic paper. As seen in the Figure 4.5, the two procedures gave two different PSDs'. This difference inferred to occurrence of high amount of organics in the grit (Neighbor and Cooper, 1965). The variation in PSD between the oven-dried grit and ignited grit became clearer when the

parameters mentioned in Table 4.3 were compared for these two sets of samples. The results are shown in Table 4.4.

Table 4.4 Results of grading parameters for oven-dried grit and ignited grit

Parameter	Grit dried at 105^0C	Grit ignited at 550^0C
D_{10} (μm)	220	170
D_{30} (μm)	500	280
D_{60} (μm)	1600	450
C_u	7.27	2.65
C_c	0.71	1.02

It can be argued that the oven-drying procedure adopted for grit preparation provided a more honest description of settled grit as opposed to the ignition procedure. Because the ignition process considerably reduced the sizes of grit particles. This reduction was more pronounced with particles larger than 200μm. An example of this difference in particle size is shown in Figure 4.6. This Figure shows the actual grit particles retained in a 4760 μm sieve during the sieve analysis of the two grit samples. Wilson et al. (2007) mentioned change in grit size distribution due to possible fracture of limestone particles present in grit during ignition at 550^0C.

Figure 4.6 Grit particles retained on 4760 μm sieve
Left – grit dried at 105^0C, Right – grit ignited at 550^0C

The effective size (D_{10}) for oven-dried grit was found 220 μm (Table 4.4) indicating only 10% of the settled grit was finer than this size. This value is in close agreement with theory which depicts that an ideal grit should mostly contain particles larger than 210 μm. A volatile solids analysis on each size fraction obtained during the sieving of oven-dried grit sample is shown in Table 4.5. This table showed that the fixed solid (%) was relatively higher for particles within the range of 594μm>d>150μm and relatively lower for particles larger than 594 μm.

Table 4.5 Results of fixed solids content (%) for different sieve fractions

Sieve size (μm)	Mass retained (%)	FS (%)
4760	14.67	26.64
2000	17.76	26.87
850	24.71	30.29
594	6.95	79.52
420	10.42	92.75
210	17.37	95.09
150	2.70	92.58
74	1.54	83.96
<74	3.47	81.24

The removal efficiency of an aerated grit chamber can be calculated at least in three different ways (Neighbor and Cooper, 1965): (a) removal of a specific size of particle, (b) removal of all particles greater than a specific size or (c) removal of all particles. This requires an extensive study of grit particles entering and leaving the system. It is also important to get a full gradation of grit that settles at the bottom. In this study, a comprehensive sampling was done on the effluent of the grit chamber. The sampling was specially designed to capture any variation in effluent composition along the depth of the chamber. Solid analyses on the effluent sample revealed the variation in a quantitative

manner. Solid analyses on grit chamber influent were also carried out. The results of suspended solids and fixed solids analyses provided more insight on the influent and effluent grit composition. The data obtained from these analyses provided a valuable baseline for future study on the pilot-scale grit chamber.

Due to instrumental limitation, it was not possible to collect samples representing the entire depth of the influent channel. Therefore, exact estimation of grit chamber's efficiency could not be determined. The results of solids analysis on grit chamber influent are shown in Table 4.6. These results represent the influent condition 0.60 m below the top water surface.

Table 4.6 Results of grit chamber influent analyses

Solids analysis	mgL^{-1}
Total solids, TS	971
Total fixed solids, TFS	558
Total volatile solids, TVS	414
Total suspended solids, TSS	237
Fixed suspended solids, FSS	140
Volatile suspended solids, VSS	97.1

Nonetheless, the results of this work provided enough parameters to check the performance of the grit chamber in qualitative ways. From solid grit sieving, it was found that 90% of the particles were above the size of 220 μm. This large percentage of coarse particles indicated that the grit chamber was functioning in an efficient manner (Neighbor and Cooper, 1965). The only concern was the moisture of the grit associated with offensive odour. This was explained by the relatively high volatile solid content present in the grit. Further analysis revealed that relatively larger particles were the main contributors to volatile solids content in grit.

It should be noted that in Gold Bar WWTP, wastewater flows directly into the grit chambers as soon as they arrive at the plant. The absence of coarse bar screen before the grit chambers allowed rags, sticks and similar other large organic wastes to appear in grit. This also attributes to the large size distribution of settled grit.

4.6 Conclusion

In this study, grit samples were collected from the aerated grit chamber # 7 at Gold Bar WWTP. Liquid samples were collected from the tank's influent and effluent channel and solid grit samples were collected from the grit bin. An extensive sampling was carried out at the effluent gate of the tank at different depths of the water column covering approximately 3.50 m below from top water surface. The liquid samples were analyzed for solid content and the solid grit sample was investigated by sieve analysis. The results were used to describe grit characteristics and to predict the performance of the aerated grit chamber. The influent grit sample had a TSS concentration of 237 mgL^{-1} and a FSS concentration of 140 mgL^{-1}. The effluent grit sample had a TSS concentration ranging from 210 mgL^{-1} to 293 mgL^{-1} while the FSS concentration varied from 126 mgL^{-1} to 176 mgL^{-1}. From sieve analysis of solid grit sample dried at 105^0C, it was found that 90% of the grit particles were above the size 220 μm. This value was in close agreement with the design basis of aerated grit chamber, which in turn, suggested that the grit chamber was functioning properly at the time of sample collection. However, results of gravimetric analysis pointed out high volatile solid content (39.25% by wt.) and high moisture content (> 50%, by wt.) of the settled grit. This explained the sloppiness and odour associated with grit and these physical properties classify the grit as type 3.

CHAPTER 5

LASER MEASUREMENTS OF HYDRAULIC JET MIXING IN PILOT-SCALE MIXING TANK

5.1 Introduction

Aerated grit chambers are conventionally designed to induce settling of inert particles by creating a circular spiral flow pattern of wastewater in the chambers. Air diffusers are located near the bottom of the grit chambers to introduce a transverse circulation of air bubbles that combines with the longitudinal wastewater flow which results in the helical motion of fluid. Usually medium to coarse bubble diffusers are used for creating the transverse circulation in grit chambers. However, Brenner and Diskin (1991) in their study on a prototype of conventional aerated grit chamber, introduced hydraulic jets instead of air diffusers for creating the transverse circulation. Full-scale operation data of four jet-circulated grit chambers at Soreq Treatment Plant, Israel were also mentioned in the closure of their paper discussion.

The application of jets and injectors in grit chambers may prove to be advantageous over conventional aerated grit chambers for the following reasons (Brenner and Diskin, 1991):

First of all, grease, fats, oils and many other surface active agents present in wastewater get attached to the inert particles and add buoyancy. Therefore, inert matter do not settle as expected which reduces the efficiency of grit chambers. The shearing force of water jets can help to strip the inert grit of the surface active agents and hence restore the original density of the grit allowing better settling. Secondly, in case of wastewater containing high volatile organic compounds, aeration in grit chamber may

result in odour nuisance and possible health risks plant operators. Application of water jets could significantly reduce this problem. Thirdly, jet-circulated grit chambers will be much easier to operate as it would not require blowers or compressed air like aerated grit chambers.

However, replacing the aeration system of a conventional grit chamber with hydraulic jets needs extensive study on how the tank's performance and hydrodynamic characteristics are influenced by such a system. Prior knowledge about water jet characteristics which primarily depend upon nozzle type, size, numbers, submergence and orientation is essential in order to predict jet dimensions and flow pattern in the tank.

In this study PLIF laser measurement technique was used to investigate concentration fields in a water tank by varying the number and arrangement of nozzles and injectors. The tank had identical width to water column depth ratio as that of pilot-scale grit chamber. The total flow rate in this tank was also in the same range as that of the pilot-scale grit chamber. Therefore, the results of this study can give important information for initial arrangements of hydraulic jets in the pilot-scale grit chamber.

5.2 Planar Laser Induced Fluorescence

Planar laser-induced fluorescence (PLIF) is a non-intrusive technique to perform planar measurements of either temperature or concentration field in liquids. The principle of this technique is to excite a fluorescent tracer dye in the fluid flow with laser light and to optically capture the resulting fluorescence emission. The measured fluorescence is then used to surmise the local dye concentration.

5.2.1 Theoretical Background

In PLIF a fluorescent dye is excited with a laser sheet within its adsorption spectrum. A fraction of the light energy is absorbed by the dye and, as a result, part of the absorbed energy is re-emitted at a longer wavelength. The fluorescence emission is then captured by video recording or still photography or by charge-coupled device (CCD) camera photography while filtering out the laser light. Crimaldi (2008) described fluorescence intensity F, as:

$$F \propto \frac{I}{1 + I/I_{saturation}} C \qquad (5.1)$$

where $I_{saturation}$ is the saturation intensity of the fluorescent, I is the excitation intensity and C is the local concentration of fluorescent. When $I \ll I_{saturation}$ then the equation reduces to the following:

$$F \propto IC \qquad (5.2)$$

This gives a simple principle to measure concentrations through experimentally determining the fluorescence intensity. According to Beer-Lambert law, when light passes through an absorbing medium the intensity I, diminishes along its line of propagation as following:

$$\frac{I(x_1)}{I(x_0)} = \exp\left[-\int_{x_0}^{x} \varepsilon C(x) dx \right] \qquad (5.3)$$

where x_1 is the direction of propagation of light from x_0, C(x) is the local dye concentration and ε is the extinction coefficient for the absorbing species which is dependent on excitation energy wavelength.

Another form of this law is

$$\frac{dI}{I} = -\varepsilon C dx \qquad (5.4)$$

If it is assumed that the dye concentration C remains uniform within the volume of dye excited by light intensity I, then from Eqs. (5.2) and (5.4) it can be shown

$$dF = \Phi \varepsilon I C dV \qquad (5.5)$$

where Φ = quantum efficiency that is ratio of emitted energy to absorbed energy, dV = dx dA, where dx is the infinitesimal length of illuminated medium and dA is the cross-sectional area perpendicular to light. Combining Eqs. (5.3) and (5.5) give

$$F(x_1) = I(x_0).\Phi.\varepsilon.C \exp(-\varepsilon l C) \qquad (5.6)$$

This is the fundamental equation used in PLIF measurements of concentration in aqueous flow at weak excitation level. A more detailed discussion on theories related PLIF and concentration measurement can be found in Walker (1987), Law and Wang (2000) and Larsen and Crimaldi (2006).

5.2.2 PLIF and Hydraulic Jets

Flow field visualization by laser and fluorescence technique has been extremely popular in the fluid mechanics community over the years. With the rapid advance in laser–induced fluorescence (LIF) measurements within the last five decades, numerous studies employing this technique on jet mixing have been reported in literature. For instance, PLIF has been applied to characterize a jet plume (Webster et al., 2003), to study the geometry of scalar iso-surfaces (Catrakis and Dimotakis, 1996) and to quantify mixing in impinging jets (Guillard et al., 1998); (Unger and Muzzio, 1999). LIF has been used to measure scalar concentration at a single point in jet centerline (Dahm and

Dimotakis, 1990), jets in 2D planes (Ferrier et al., 1993), and turbulent jets in 3D planes (Xiaodong and Roberts, 2003). The PLIF technique has been coupled with digital particle image velocimetry (PIV) for simultaneous measurement of concentration and/or temperature and velocity fields for turbulent jets (Sakakibara et al., 1997); (Webster et al., 2001); (Borg et al., 2001); (Chang and Cowen, 2002); (Feng et al., 2005). Round jets issuing into a uniform opposing has been investigated for mean concentration and flow visualization by Yoda and Fiedler (1996) and turbulent transport in a stirred tank with arrays of jets at the bottom was explained in Variano and Cowen (2008).

5.3 Experimental Equipment

5.3.1 PLIF Instrumentation

The PLIF system fundamentally consists of a fluorescent dye to tag the fluid, laser source to illuminate the area of interest, a CCD camera system to capture the fluorescence emission and a post processing system for image acquisition and analysis.

5.3.1.1 Fluorescent Dye

In this PLIF study, Rhodamine 6G (Rh6G) (molecular formula: $C_{28}H_{31}N_2O_3Cl$, molecular weight: 479.02 g/mol) was used as the as the scalar surrogate in fluid flow. This dye is highly soluble in water and possesses quantum efficiency greater than 95%. This allows a very high fluorescence signal acquisition during laser experiments. The spectral characteristics of Rh6G also makes it an excellent choice for experiments with Nd:YAG laser. The absorption spectrum of Rh6G ranges from 460 to 560 nm with peak at 530 nm (Webster et al., 2001). This is in perfect harmony with Nd:YAG laser which

functions at 532 nm wavelength. The emission spectrum of Rh6G ranges from 540 to 640 nm with peak at 555 nm (Penzkofer and Leupacher, 1987). The dye shows remarkable resistance to photo-bleaching (Larsen and Crimaldi, 2006) which ensures the accuracy of signals obtained at high laser energy. Moreover, Rh6G is reported to possess high chemical stability which enables long storage of its high concentration solution without compromising the chemical integrity.

During PLIF study, it is crucial to record only the emitted fluorescence while filtering out the excitation light (laser). Otherwise, the scattered laser would interfere with the measured concentration scalar and appear as false high concentration pixels in post processing. In this study, an optical filter with cut-off around 560 nm was used to isolate the green Nd:YAG laser light from yellow/orange fluorescence emission of Rh6G.

5.3.1.2 Laser Source

Nd:YAG pulsed laser is getting increasingly popular due to their high energy per image exposure as opposed to ion lasers with continuous but weak output (Karasso and Mungal, 1997). The only major drawback of laser sheets generated by Nd:YAG laser is their non-uniformity (spatial variation) of energy distribution and pulse-to-pulse fluctuations in laser energy (Law and Wang, 2000). A New Wave Research Solo Nd:YAG pulsed laser was used in this study to create a laser sheet illuminating a planar cross- section within the flow. The laser has an output beam diameter 4.5 mm and is designed to operate at 532 nm with ± 4% pulse stability. In this experiment 532 nm wavelength was utilized with pulse length of 10 ns. The time delay between pulses was set to 100 μs with maximum repetition rate of 8 Hz.

5.3.1.3. CCD Camera and Image Processing

A digital CCD camera (Hamamatsu C8484-05C) equipped with Nikon lens was used to capture PLIF images. The camera produced 12 bit digital images with 1344 horizontal and 1024 vertical pixels. The images were recorded with single frame configuration at a time interval of 1000 ms. An orange optical filter was placed in front of the camera lens to allow only the emitted fluorescence to be imaged. A FlowMap System Hub® (Dantec Dynamics) was used for image acquisition and transfer to a computer where FlowMap Software® (Dantec Dynamics) was used for processing the images to quantify the concentration profile of the system.

5.3.2 Flow Equipment

5.3.2.1 Injectors and Nozzles

In this experiment a total of eight Mazzei injectors of model A-3 and eight Mazzei mixing nozzles with jet diameter d_j = 5.3 mm were used. Each nozzle was driven by an injector and the injectors were connected to the pump through manifold. The nozzle-injector arrangement was made in such a way that allowed each jet to operate individually. Geometric dimensions of the injector and nozzle are given in Figure 5.1.

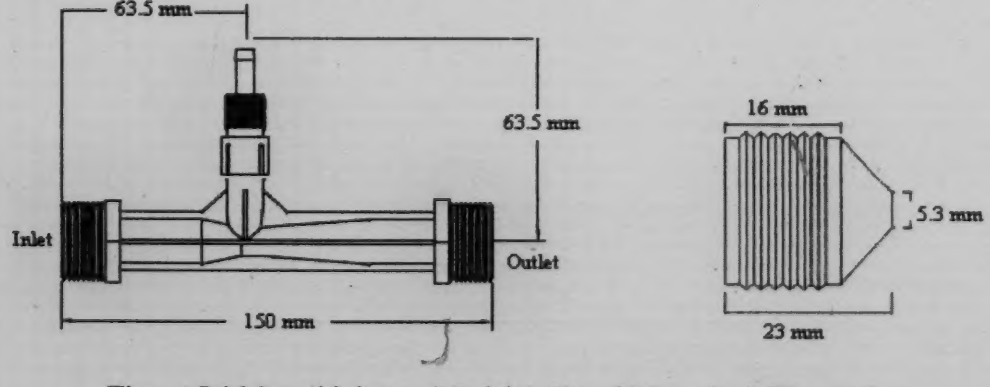

Figure 5.1 Mazzei injector (Model A-3) and Mazzei mixing nozzle

The injectors were designed to offer a motive flow rate (Q_{inj}) of 7.57 $\times 10^{-5}$ m^3s^{-1} at 138 kPa (1.2 gpm at 20 psi). In this condition, jet velocity u_j ($= \frac{Q_{inj}}{0.25\pi d_j^2}$) was 3.43 ms^{-1} and jet Reynolds number Re_j was 13.90×10^3. Re_j defined as $Re_j = \frac{d_j u_j \rho}{\mu}$; where ρ and μ corresponded to water density and viscosity at the experimental condition (10^0C).

5.3.2.2 Pilot-scale Mixing Tank

The mixing tank was made of clear acrylic with the following dimensions L×W×H = 427 mm×427 mm×436 mm. Water column depth was maintained at 386 mm in order to keep the width to water depth ratio (1.1:1) of this tank equal to that of the pilot-scale grit chamber. The total water flow rate in the tank was maintained from 3.45 $\times10^{-3}$ to 3.49 $\times10^{-3}$ m^3s^{-1}, close to the pilot-scale grit chamber operation. These similarities in designing the mixing tank were maintained for two reasons. First, the experimental findings with water jets in this mixing tank can serve as a baseline for initial arrangements of jets in the pilot grit chamber. Secondly, in case of constructing a prototype / full-scale mixing tank with hydraulic jets preceding the full-scale aerated grit chamber, this pilot model can be scaled-up easily while maintaining a balance with the hydraulic flow rate of the grit chamber.

The mixing tank was designed to hold jets at three different depths on both side walls. Each side wall was designed to hold a maximum of 12 jets with 4 jets at each depth. This allowed side jets to be tested under opposing (jets facing each other from opposite side walls) and alternating (jets facing each other but apart with a distance of 80 mm) arrangements. Engineering drawings of the mixing tank design are shown in Figure 5.2. Figure 5.3 shows the laser equipment used for PLIF study.

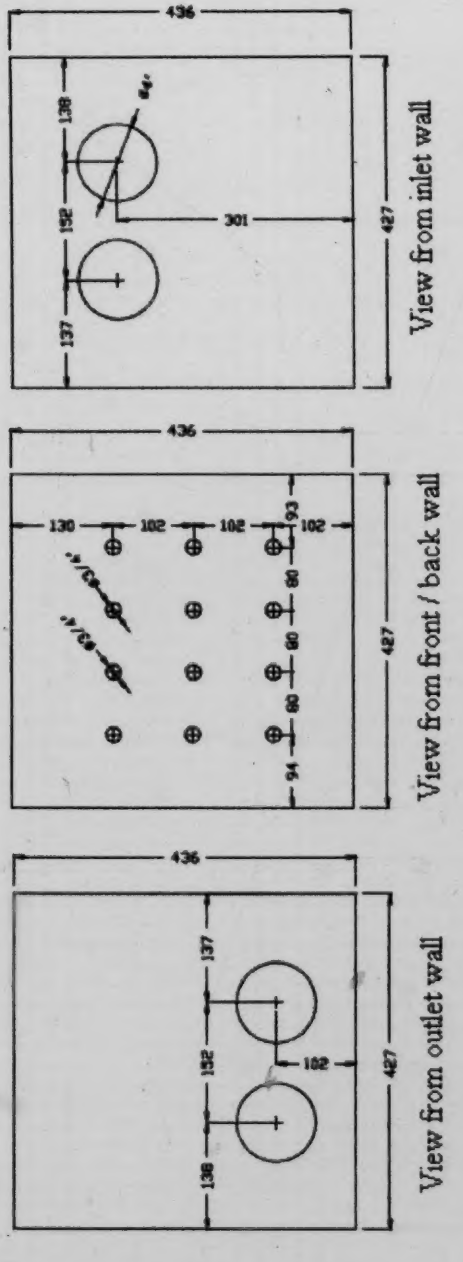

Figure 5.2 Layout of the mixing tank designed to facilitate various jet assemblies (all dimensions are in mm)

Figure 5.4 shows the injector manifolds and jet assembly in the mixing tank. The laser-CCD camera arrangement during PLIF study is also shown in this Figure.

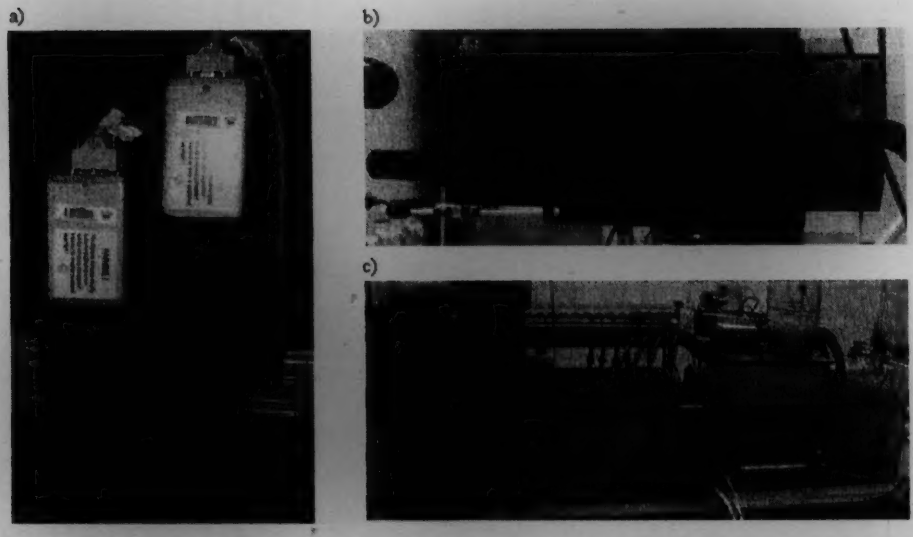

Figure 5.3 PLIF Instruments: a) CCD camera; b) Nd:YAG laser source; c) Laser controller, FlowMap System Hub® and traverse controller (from left to right)

Figure 5.4: Experimental setup: a) 8-jets assembly in mixing tank; b) Injectors assembly in manifold; c) Laser positioned parallel to flow; d) CCD camera positioned on top.

5.4 Experimental Setup and Methodology

5.4.1 PLIF Calibration

To address the response of camera pixel to varying concentration and laser energy, calibration was performed on PLIF system by filling the mixing tank with different concentrations of Rh6G solution and measuring the re-emitted fluorescence by exciting the dye at different intensities of laser energy. Concentration of Rh6G was varied from 0 to 500 μgL^{-1} and laser energy level was varied from 50 to 350 mJ. Each concentration was excited with the lowest energy first and intensity was gradually increased to the highest level. Based on the calibration images, concentrations vs. laser intensity were plotted and a least square fit was performed using the FlowMap Software®. The objective was to obtain a linear response of light intensity to concentration at the best possible resolution for the specific laser, camera and the geometric setup. This would insure weak excitation of dye tracer which infers that both quantum yield and extinction coefficient are constant. The calibration showed highest correlation coefficient of 0.86 at 300 mJ laser at a maximum Rh6G concentration of 120 μgL^{-1}. Therefore, 300 mJ energy level was used for the experiment.

5.4.2 Image Acquisition

In this experiment, mixing of water jets was observed by varying the number of jets from 2 to 8. Jets were placed 102 mm above the tank bottom on both side walls. In total four opposing assembly and two alternating arrangements were tested. The total volumetric flow rate in the tank was maintained at approximately 3.47×10^{-3} m^3s^{-1} with side jet streams varying from approximately 4 % to17 %. Two centrifugal pumps were

used, one for driving water through the tank inlet and the other for jet streams, and the flow rates were recorded by F-1000-RB flow meters (Blue-White® Industries). Exact operational parameters for jet experiment are summarized in Tables 5.1 and 5.2.

When the system reached steady state, a step input of Rh6G tracer dye was introduced at a rate of 3×10^{-6} m^3s^{-1} at the tank inlet. A tracer concentration of 56 mgL^{-1} was used to yield an average concentration of 49μgL^{-1} when fully mixed with the total liquid flow (3.47×10^{-3} m^3s^{-1}) in the tank. This concentration was within the range of linear relation for PLIF calibration. During the PLIF study, laser sheet was introduced from the side wall of the tank illuminating a horizontal cross-sectional plane and CCD camera was placed near the tank outlet to capture images from the top of the water surface. For each operating condition, PLIF image acquisition duration was 30 seconds. Duplicate images were taken for each jet arrangement to reduce any uncertainty associated with the measurements.

Table 5.1 Summary of the operating parameters of jet experiments

No. of jets	Jet array	Jets flow rate, Q_J (m^3s^{-1})	Total flow rate, Q_L (m^3s^{-1})	Q_J / Q_L (%)
2	Opposing	1.5×10^{-4}	3.49×10^{-3}	4.3
4	Opposing	3.0×10^{-4}	3.47×10^{-3}	8.5
6	Opposing	4.5×10^{-4}	3.47×10^{-3}	13.0
8	Opposing	6.0×10^{-4}	3.47×10^{-3}	17.4
2	Alternating	1.5×10^{-4}	3.46×10^{-3}	4.4
4	Alternating	3.0×10^{-4}	3.45×10^{-3}	8.8

Jet-injector specification	Values
Jet diameter (mm)	5.3
Jet velocity (ms^{-1})	3.43
Injector motive flow rate (m^3s^{-1})	7.57×10^{-5}
Jet Reynolds no., Re_{jet}	13.90×10^{3}

Table 5.2 Operating conditions for PLIF instruments

Parameters	Value
Laser wavelength	532 nm
Pulse energy	300 mJ
Pulse repetition rate	8 hz
No. of recordings per run	30
Time between recording	1000 ms
Pulse duration	0.01μs
Time between pulses	100 μs

5.4.3 Tracer study with KCl

In order to validate the PLIF measurements, tracer studies were performed at each experimental setup by keeping the operational parameters the same. A step input of 0.5M Potassium chloride (KCl) was introduced at the inlet of the mixing tank and conductivity was measured at the outlet of the tank using YSI Model 34 Conductance Resistance Meter and YSI 3417 conductivity cell.

5.5 Results and Discussion

Raw images of PLIF were processed and re-sampled in FlowMap Software® based on the calibration curve to obtain scalar maps of concentration distribution of the tracer dye along the horizontal cross-section parallel to the fluid flow. These scalar maps revealed the instantaneous distribution and variability in concentration within the fluid flow. Concentrations were represented in colour codes where highest dye concentrations were assigned green and orange, and lowest dye concentrations were assigned magenta and violet. On this scale better, mixing was represented in purple and/or blue.

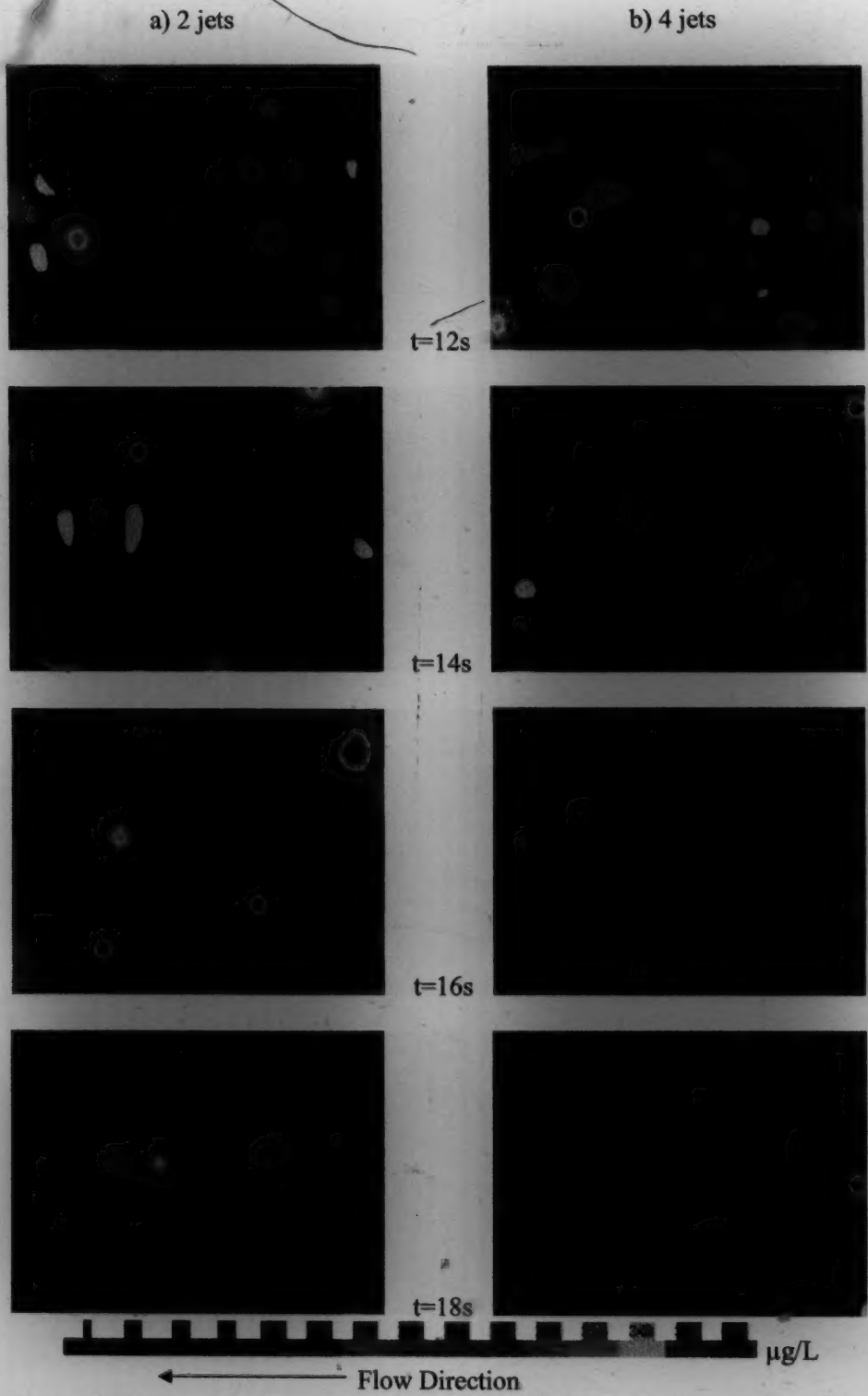

Figure 5.5 Sequence of instantaneous concentration variation during jets mixing

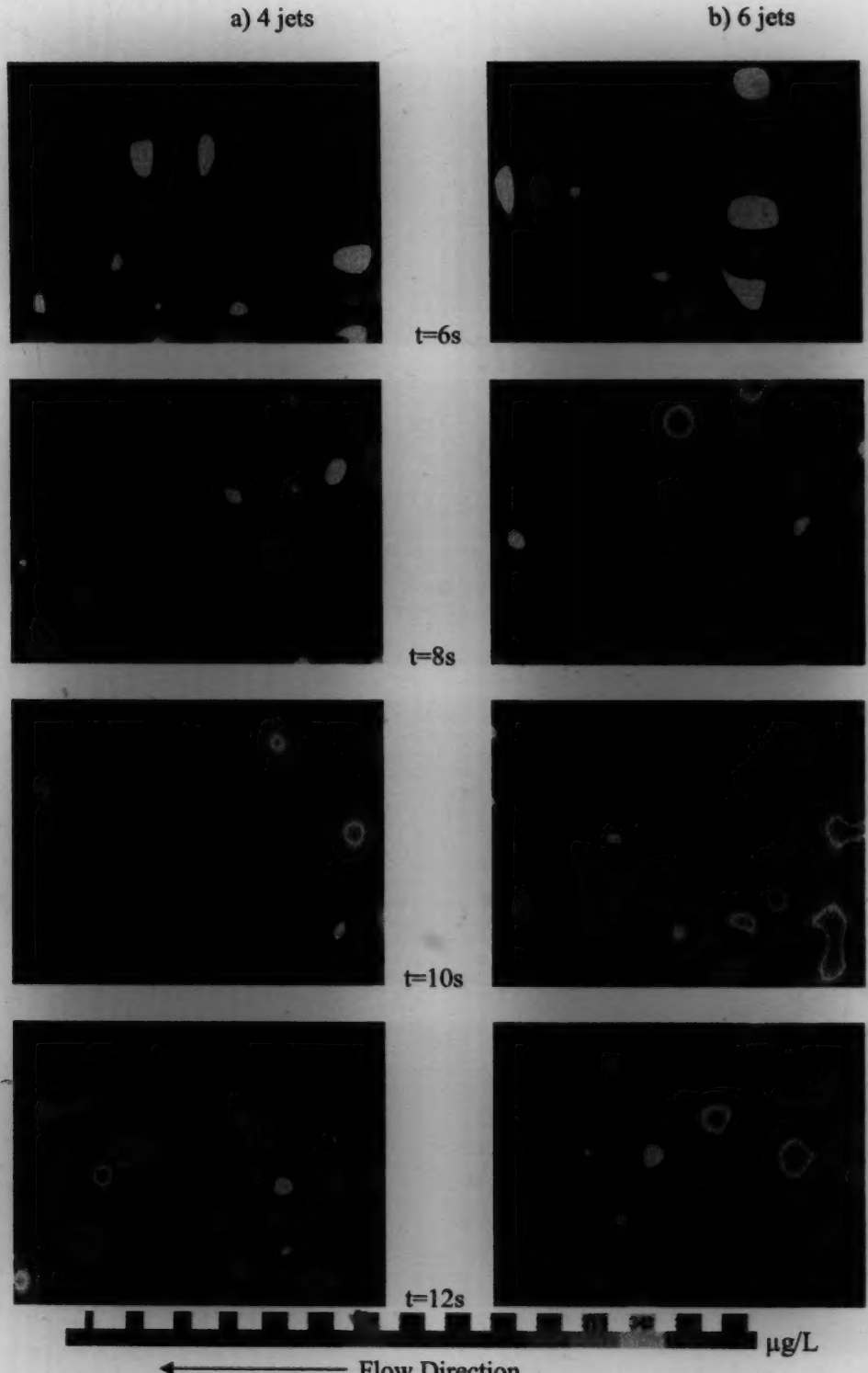

Figure 5.6 Sequence of instantaneous concentration variation during jets mixing

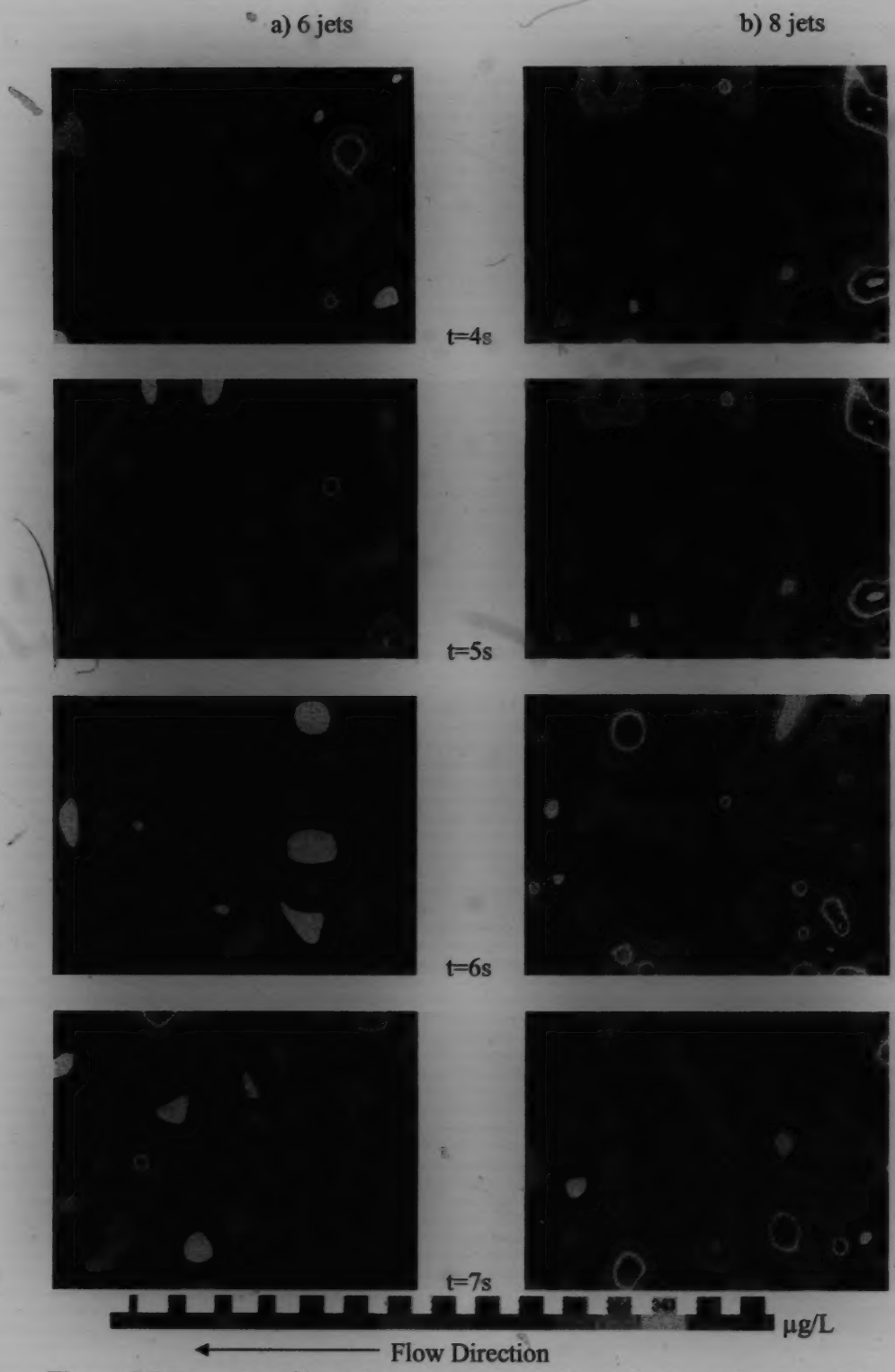

Figure 5.7 Sequence of instantaneous concentration variation during jets mixing

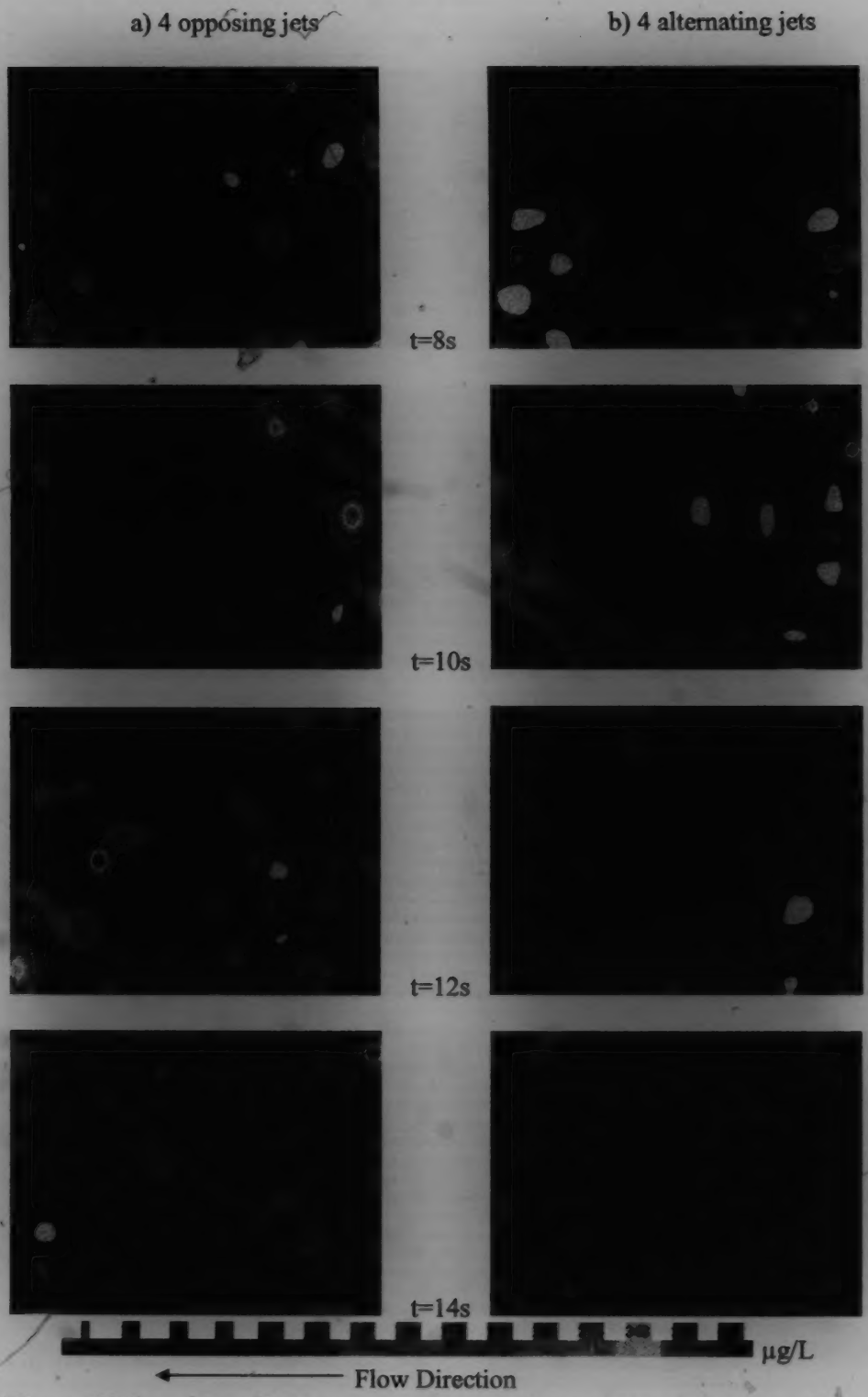

Figure 5.8 Sequence of instantaneous concentration variation during jets mixing

The scalar concentration variations influenced by increasing number of jets are presented in Figures 5.5 to 5.8. With 4 jets (placed near the tank inlet in opposing arrangement), the concentration distributions were more homogenous than those found with 2 jets as shown in Figure 5.5. At 14 sec. the dye concentrations in 2 jet arrangement were mostly within the range of 29-56μgL^{-1} with some regions with near zero concentration. With 4 jet arrangements, the dye concentration was mostly uniform and varied within the range of 86-113μgL^{-1}. This indicated a relatively better mixing with 4 jets as compared to 2 jets. Next the concentration profiles of 4 and 6 jet arrangements were compared as shown in Figure 5.6. The concentration maps for these two setups were similar up to 8 sec; however, at 10 s a burst of high dye concentration (green color) was noticed over a large area which quickly passed the region of measurement in 6 jet arrangements. No such burst of high tracer concentration was observed with 4 jet arrangement. In fact, more uniformity (blue color) in concentration distribution was perceived with 4 jets setup than the 6 jets arrangement. Similar comparisons between 6 and 8 jet arrangements are shown in Figure 5.7. A well mixed region (blue color) of dye tracer with concentration was observed almost instantaneously when 8 jets were placed covering the entire length of the tank. However, the dye concentration increased rapidly to around 200-342 μgL^{-1} within a very short period (2 sec). For both setups (6 and 8 jets) multiple fluctuations in dye concentration was observed over the entire period of image acquisition. Comparison of the PLIF scalar maps for the above four setups (2, 4, 6 and 8 jets in opposing position) showed that a relatively uniform concentration distribution was achieved when 4 jets were placed near the inlet of mixing tank. High variability in

instantaneous concentration distribution was demonstrated when jet numbers were increased to six and eight.

To explore the spatial distribution of jets in mixing tank, four sets of experiments were performed with 2 and 4 jets placing them in either opposing (directly facing each other) and alternate (facing each other from a distance apart) positions. Examples of re-sampled images for 4 jets in opposing and alternating positions are presented in Figure 5.8. In the opposing position, two jets were placed on each side wall 80 mm apart and in alternating position, the two jets on each side wall were 160 mm apart. In this way, the alternating arrangement covered the entire tank length while opposing arrangement covered only half of the tank length. The concentration maps for the two setups were fairly similar except that a relatively uniform dye concentration was achieved slightly faster in opposing jets assembly than the alternating positions.

While the coloured scalar maps provided a qualitative depiction of mixing efficiency, these images were further analyzed to quantify these concentration maps. This was done by converting each and every pixel of the scalar images to its corresponding numerical concentration values by using the FlowMap Software®. Conversion of re-sampled PLIF images to such concentration values also gave information on sequential change in dye concentration in any region of interest. This information was used to generate residence time distribution (RTD) for step input of Rh6G tracer for each experimental setup. The curve is known as F-curve which goes from 0 to 1 and represents the fraction of step change in input tracer concentration at the point of measurement up to time t (Digiano et al., 2005). The analytical expression for F is given by $F = \frac{C_t}{C_0}$ (5.7)

where, C_t represents tracer concentration at time t and C_0 represents initial mixed tracer concentration. An example of F-curve obtained from tracer concentration shown in PLIF images for 4 opposing jets arrangement is shown in Figure 5.9.

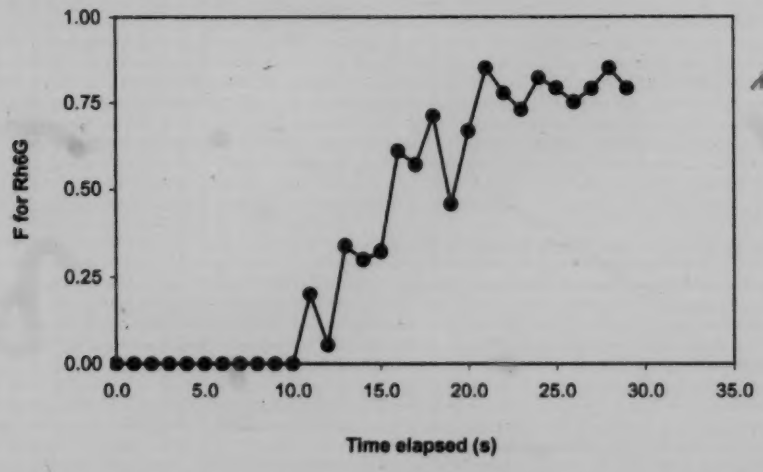

Figure 5.9 F-curve for mixing tank with 4 opposing jets (calculated from PLIF images).

In order to double check the PLIF concentration measurements, F-curves were constructed for each jet experiment in identical operating parameters (i.e. jet number, jet arrangement, jet flow rate, total flow rate) using step input of KCl . Figure 5.10 shows the F-curve from the KCl tracer study obtained for 4-opposing jet arrangements.

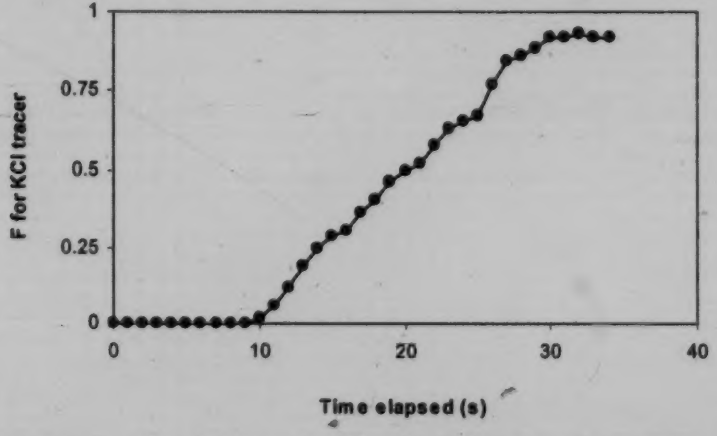

Figure 5.10 F-curve for mixing tank with 4 opposing jets (from KCl tracer study)

As seen in Figures 5.9 and 5.10, both curves showed a time lag of 10 sec at the beginning before tracer concentration can be detected at the tank outlet. The time lag was followed by a sharp increase in concentration to approach the initial mixed tracer concentration C_0. A mass balance of tracer was carried out around the system to check the consistency of the experiments and showed 88% recovery of Rh6G and 100% recovery of KCl at the tank outlet.

It is known that F-curves often tend to smooth over some of the details in flow condition (Levenspiel, 1996). This can explain the rather smooth F-curve (Figure 5.10) obtained from the step input of KCl tracer. There were some small peaks present in that curve, though, they can often remain unnoticed if not scrutinized carefully enough. On the contrary, the F-curve acquired from PLIF study (Figure 5.9) captured those rises quite successfully. Those multiple peaks referred to existence of possible strong recirculation and/or channelling within the mixing tank. This was quite expected as jets would invariably cause forward and backward mixing, in the near-field and far-field region, respectively, when introduced in counter-flow (Yoda and Fiedler, 1996).

The mean residence time, $\bar{t}$ and variance, σ^2 for the tracer response were calculated according to Levenspiel, (1996) using the following equations.

$$\bar{t} = \frac{\sum_{i=1}^{n} (2\Delta C_{max} - C_{i-1} - C_i)(t_i - t_{i-1})}{2\Delta C_{max}} \qquad (5.8)$$

$$\sigma^2 = \frac{\sum_{i=1}^{n} (t_{i-1} + t_i)(t_i - t_{i-1})(2\Delta C_{max} - C_{i-1} - C_i)}{2\Delta C_{max}} \qquad (5.9)$$

where ΔC_{max} is the difference between initial and final tracer concentration. Table 5.3 summarizes the theoretical hydraulic retention time and the observed mean residence

time and variance for both KCl tracer study and Rh6G tracer response extracted from PLIF study. The mean residence for the PLIF study was smaller by 4 sec than that of the KCl study. The variance was in close proximity for both studies. These results help to establish the validity of PLIF study for measuring the scalar concentration and describing the hydraulic jet mixing in the pilot-scale mixing tank.

Table 5.3 Mean and variance of tracer response for mixing tank operating with 4 opposing jets

Parameters	KCl tracer study	Rh6G PLIF study
Hydraulic residence time, (s)	20.23	20.23
Mean residence time, (s)	20.26	18.06
Variance (s^2)	42.07	42.31

Another way of analyzing the jet mixing phenomena was to compare the magnitude of dispersion in terms of axial dispersion number for each operating conditions (Baawain, 2007). Axial dispersion number, N_D is a dimensionless number defined as

$$N_D = \frac{D_L}{uL} \qquad (5.10)$$

where D_L is the longitudinal dispersion coefficient, u is the fluid velocity and L is the characteristic length in axial direction. The dispersion number can be calculated from variance and mean of pulse tracer response under different boundary conditions (Levenspiel, 1996). For closed open system, the relation is as follows

$$\sigma_\theta^2 = \frac{\sigma^2}{\left(\bar{t}\right)^2} = 2\frac{D_L}{uL} + 3\left(\frac{D_L}{uL}\right)^2 \qquad (5.11)$$

For this study, the tracer response data extracted from PLIF images were converted to pulse tracer response through differentiation and the variance and mean were

calculated from linear interpolation as stated in Levenspiel (1996). Then the dispersion number was calculated from Eqn. (5.11). For the mixing tank operation, the closed open boundary condition was chosen because the tracer entered the mixing tank in plug-flow condition and the flow became dispersed at the point of measurement (CCD camera position). The calculated dispersion numbers were plotted against the number of jets and this is shown in Figure 5.11.

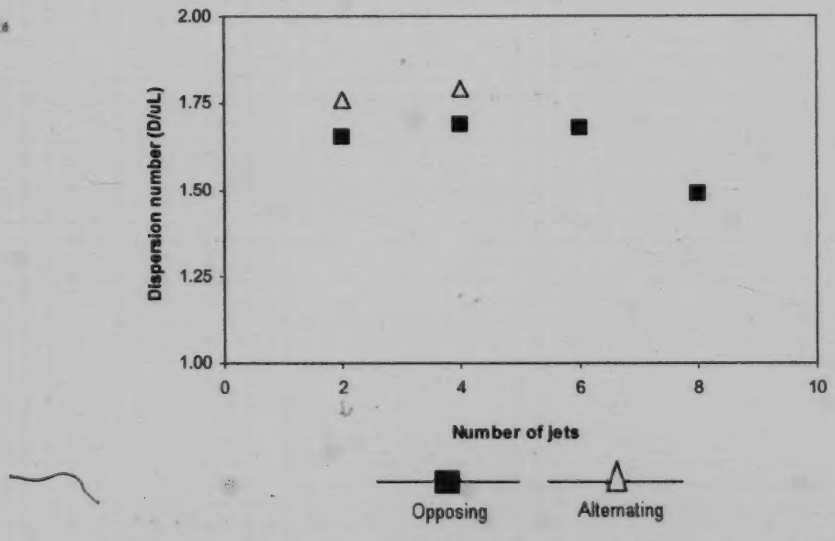

Figure 5.11 Change in dispersion number with number of jets

It was observed that the magnitude of dispersion increased with increase in jet numbers up to 6 jets in opposing jet arrangement. Maximum dispersion was obtained with 4 jets arrangement ($N_D = 1.69$). Then with 8 jets arrangement the dispersion number reduced to a value of 1.49. It was also observed that for same number of jets, each time the alternating arrangement gave a higher dispersion value than opposing arrangement. The 4 jets in alternating position achieved maximum dispersion of all the experimental setup corresponding to a dispersion number of 1.79. The opposing arrangement with 4 jets covered the entire length of the tank, while the same number of jets when placed in

opposing position covered only half of the tank length. This may be the reason for better axial dispersion achieved in alternative arrangement of jets than the opposing assembly.

From the above discussions, it is evident that PLIF images acquired in this study contained a lot of information to improve the understanding of flow behaviour and mixing phenomena within the pilot-scale mixing tank. These images showed the potentiality of describing flow behaviour in great detail and with much more accuracy. Future work is required for better interpretation of results for understanding the effects of jet number and jet arrangement and optimizing the mixing phenomena.

5.6 Conclusion

In this study, a pilot-scale mixing tank was studied with hydraulic jets and planar laser-induced fluorescence technique was implemented to investigate the mixing performance of nozzle-injectors based on instantaneous scalar concentration maps. The coloured scalar concentration maps showed better uniformity in concentration profile was achieved with four jets. The PLIF images were further processed and fluorescence tracer response was acquired showing the flow pattern inside the tank. The tracer responses were compared with KCl responses obtained from conventional tracer study. Both responses were in close agreement which indicated the validity of PLIF data. An attempt was made to quantify the mixing phenomena in terms of dimensionless axial dispersion number. The analyses indicated highest axial dispersion was achieved inside the tank with four jet-injectors. Arranging the jets in alternative positions provided better axial dispersion corresponding to a dispersion number of 1.79.

CHAPTER 6

GENERAL CONCLUSIONS

In this work, a pilot-scale aerated grit chamber was designed and constructed to replicate the flow conditions of the full-scale aerated grit chamber # 7 at Gold Bar WWTP. The model was built to a 15:1 scale and the Froude number similitude criterion was employed to maintain geometric, kinematic and dynamic similitude between the model and full-scale unit.

Analysis of the tracer responses revealed that the non-ideal flow pattern inside the pilot-scale model was best described by nine-tanks in series model. The axial dispersion model showed a dispersion value of 5.95×10^{-2}.

In this study, extensive sampling was carried out near the outlet of the full-scale aerated grit chamber to capture the depth wise variation of solid content at the effluent stream. The influent contained 237 mgL^{-1} of TSS and 140 mgL^{-1} FSS. The effluent grit sample had a TSS concentration ranging from 210 mgL^{-1} to 293 mgL^{-1} while the FSS concentration varied from 126 mgL^{-1} to 176 mgL^{-1}. Results of wet sieve analysis showed 90% of the settled grit was above the size 220 μm.

The PLIF study on the pilot-scale mixing tank described the hydraulic jet mixing phenomena in terms of instantaneous scalar concentration maps. Highest degree of axial dispersion was obtained with 4 jet–injectors operating in alternative arrangement. The corresponding axial dispersion number was 1.79.

Further studies are required to generalize the optimum number of jets and their orientation in the mixing tank and to resolve scale up issues of this vessel. Jets can be incorporated in the pilot scale grit chamber as well. PLIF measurements will prove to be

valuable for this kind of study for developing knowledge about jet mixing and reactor hydrodynamics, eventually facilitating an early determination of process parameters for water-jet operated grit chamber.

REFERENCES

Albrecht, A. E. (1967). "Aerated Grit Operation Design and Chamber." *Water and Sewage Works*, **114**(9), 331-335.

American Public Health Association, American Water Works Association and Water Environment Federation. (1999). Standard Methods for the Examination of Water and Wastewater. American Public Health Association, Washington.

Baawain, M. S. A. (2007). "Investigating Environmental Engineering Reactors Using Laser Measurement Techniques and Advanced Modelling." Ph.D. thesis Department of Civil and Environmental Engineering,*University of Alberta*.

Battaglia, A., Fox, P. and Pohland, F. G. (1993). "Calculation of Residence Time Distribution from Tracer Recycle Experiments." *Water Research*, **27**(2), 337-341.

Borg, A., Bolinder, J. and Fuchs, L. (2001). "Simultaneous Velocity and Concentration Measurements in the near Field of a Turbulent Low-Pressure Jet by Digital Particle Image Velocimetry-Planar Laser-Induced Fluorescence." *Experiments in Fluids*, **31**(2), 140-152.

Brenner, A. and Diskin, M. H. (1991). "Model Study of Jet-Circulated Grit Chamber." *Journal of Environmental Engineering*, **117**(6), 782-787.

Catrakis, H. J. and Dimotakis, P. E. (1996). "Mixing in Turbulent Jets: Scalar Measures and Isosurface Geometry." *Journal of Fluid Mechanics*, **317**, 369-406.

Chang, K.-A. and Cowen, E. A. (2002). "Turbulent Prandtl Number in Neutrally Buoyant Turbulent Round Jet." *Journal of Engineering Mechanics*, **128**(10), 1082-1087.

Chasick, A. H. and Burger, T. B. (1964). "Using Graded Sand to Test Grit Removal Apparatus." *Water Pollution Control Federation*, **36**(7), 884-894.

Crimaldi, J. P. (2008). "Planar Laser Induced Fluorescence in Aqueous Flows." *Experiments in Fluids*, **44**(6), 851-863.

Dahm, W. J. A. and Dimotakis, P. E. (1990). "Mixing at Large Schmidt Number in the Self-Similar Far Field of Turbulent Jets." *Journal of Fluid Mechanics*, **217**299-330.

DiGiano, F. A., Zhang, W. and Travaglia, A. (2005). "Calculation of the Mean Residence Time in Distribution Systems from Tracer Studies and Models." *Journal of Water Supply: Research and Technology - AQUA*, **54**(1), 1-14.

Ettema, R. (2000). Hydraulic Modeling : Concepts and Practice. Reston, VA, ASCE.

Feng, H., Olsen, M. G., Liu, Y., Fox, R. O. and Hill, J. C. (2005). "Investigation of Turbulent Mixing in a Confined Planar-Jet Reactor." *AIChE Journal*, **51**(10), 2649-2664.

Fernandez-Sempere, J., Font-Montesinos, R. and Espejo-Alcaraz, O. (1995). "Residence Time Distribution for Unsteady-State Systems." *Chemical Engineering Science*, **50**(2), 223-230.

Ferrier, A. J., Funk, D. R. and Roberts, P. J. W. (1993). "Application of Optical Techniques to the Study of Plumes in Stratified Fluids." *Dynamics of Atmospheres and Oceans*, **20**(1-2), 155-183.

Finger, R. E. and Parrick, J. (1980). "Optimization of Grit Removal at a Wastewater Treatment Plant." *Water Pollution Control Federation*, **52**(8), 2106-2116.

Guillard, F., Fritzon, R., Revstedt, J., Traegardh, C., Alden, M. and Fuchs, L. (1998). "Mixing in a Confined Turbulent Impinging Jet Using Planar Laser-Induced Fluorescence." *Experiments in Fluids*, **25**(2), 143-50.

Head, K. H. (1980). Manual of Soil Laboratory Testing. Pentech Press, London.

http://www.matweb.com/search/DataSheet.aspx?MatGUID=3cb08da2a0054447a3790015b7214d07. August 31, 2008.

Joint Committee of the American Society of Civil Engineers and the Federation of Sewage and Industrial Wastes Associations. (1959). Sewage Treatment Plant Design. New York, N.Y.

Joint Task Force of the American Society of Civil Engineers and the Water Environment Federation. (1992). Design of Municipal Wastewater Treatment Plants. Water Environment Federation ; American Society of Civil Engineers. Alexandria, Va. New York, N.Y.

Joshi, J. B. and Ranade, V. V. (2003). "Computational Fluid Dynamics for Designing Process Equipment: Expectations, Current Status, and Path Forward." *Industrial and Engineering Chemistry Research*, **42**(6), 1115-1128.

Karasso, P. S. and Mungal, M. G. (1997). "Plif Measurements in Aqueous Flows Using the Nd:Yag Laser." *Experiments in Fluids*, **23**(5), 382-7.

Kulkarni, A. A., Gorasia, A. K. and Ranade, V. V. (2007). "Hydrodynamics and Liquid Phase Residence Time Distribution in Mesh Microreactor." *Chemical Engineering Science*, **62**(24), 7484-93.

Larsen, L. G. and Crimaldi, J. P. (2006). "The Effect of Photobleaching on Plif." *Experiments in Fluids*, **41**(5), 803-12.

Law, A. W.-K. and Wang, H. (2000). "Measurement of Mixing Processes with Combined Digital Particle Image Velocimetry and Planar Laser Induced Fluorescence." *Experimental Thermal and Fluid Science*, **22**(3), 213-229.

Levenspiel, O. (1996). The Chemical Reactor Omnibook., Distributed by OSU Book Stores, Corvallis, OR.

Liu, D. H. F. and Liptâak, B. G. (2000). Wastewater Treatment. Boca Raton, FL, Lewis Pub.

Martin, A. D. (2000). "Interpretation of Residence Time Distribution Data." *Chemical Engineering Science*, **55**(23), 5907-5917.

Morales, L. and Reinhart, D. (1984). "Full-Scale Evaluation of Aerated Grit Chambers." *Journal Water Pollution Control Federation*, **56**(4), 337-343.

Nauman, E. B. (2004). Residence Time Distributions. Handbook of Industrial Mixing : Science and Practice. Wiley-Interscience, Hoboken, N.J.: 1–17 p.

Neighbor, J. B. and Cooper, T. W. (1965). "Design and Operation Criteria for Aerated Grit Chambers." *Water and Sewage Works*, **112**(12), 448-454.

Olivet, D., Valls, J., Gordillo, M. A., Freixo, A. and Sanchez, A. (2005). "Application of Residence Time Distribution Technique to the Study of the Hydrodynamic Behaviour of a Full-Scale Wastewater Treatment Plant Plug-Flow Bioreactor." *Journal of Chemical Technology and Biotechnology*, **80**(4), 425-432.

Penzkofer, A. and Leupacher, W. (1987). "Fluorescence Behaviour of Highly Concentrated Rhodamine 6g Solutions." *Journal of Luminescence*, **37**(2), 61-72.

Robinson, B. A. and Tester, J. W. (1986). "Characterization of Flow Maldistribution Using Inlet-Outlet Tracer Techniques: An Application of Internal Residence Time Distributions." *Chemical Engineering Science*, **41**(3), 469-483.

Sakakibara, J., Hishida, K. and Maeda, M. (1997). "Vortex Structure and Heat Transfer in the Stagnation Region of an Impinging Plane Jet (Simultaneous Measurements of

Velocity and Temperature Fields by Digital Particle Image Velocimetry and Laser-Induced Fluorescence)." *International Journal of Heat and Mass Transfer*, **40**(13), 3163-76.

Sawicki, J. M. (2004). "Aerated Grit Chambers Hydraulic Design Equation." *Journal of Environmental Engineering*, **130**(9), 1050-1058.

Smith, L. C., Elliot, D. J. and James, A. (1993). "Characterization of Mixing Patterns in an Anaerobic Digester by Means of Tracer Curve Analysis." *Ecological Modelling*, **69**(3-4), 267-285.

Tchobanoglous, G., Burton, F. L., Stensel, H. D. and Metcalf & Eddy. (2003). Wastewater Engineering : Treatment and Reuse. Boston, McGraw-Hill.

Unger, D. R. and Muzzio, F. J. (1999). "Laser-Induced Fluorescence Technique for the Quantification of Mixing in Impinging Jets." *AIChE Journal*, **45**(12), 2477-2486.

Variano, E. A. and Cowen, E. A. (2008). "A Random-Jet-Stirred Turbulence Tank." *Journal of Fluid Mechanics*, **604**, 1-32.

Walker, D. A. (1987). "A Fluorescence Technique for Measurement of Concentration in Mixing Liquids." *Journal of Physics E (Scientific Instruments)*, **20**(2), 217-24.

Webster, D. R., Rahman, S. and Dasi, L. P. (2003). "Laser-Induced Fluorescence Measurements of a Turbulent Plume." *Journal of Engineering Mechanics*, **129**(10), 1130-1137.

Webster, D. R., Roberts, P. J. W. and Ra'ad, L. (2001). "Simultaneous Dptv/Plif Measurements of a Turbulent Jet." *Experiments in Fluids*, **30**(1), 65-72.

Wilson, G., Tchobanoglous, G. and Griffiths, J. (2007). The Grit Book, EUTEK Systems, Inc.

Xiaodong, T. and Roberts, P. J. W. (2003). "A 3d Lif System for Turbulent Buoyant Jet Flows." *Experiments in Fluids*, **35**(6), 636-47.

Yoda, M. and Fiedler, H. E. (1996). "The Round Jet in a Uniform Counterflow: Flow Visualization and Mean Concentration Measurements." *Experiments in Fluids*, **21**(6), 427-36.

APPENDIX A

RAW DATA OF TRACER STUDY ON PILOT-SCALE GRIT CHAMBER

Table A 1: KCl tracer response in pilot-scale grit chamber

with aeration				without aeration			
Run 1		Run 2		Run 1		Run 2	
Time s	KCl Conc. mg/L	Time s	KCl Conc. mg/L	Time S	KCl Conc. mg/L	Time s	KCl Conc. mg/L
25	0.00	0	0.00	25	0.00	25	0.00
36	0.00	14	0.70	29	1.41	29	1.41
38	0.70	36	0.70	36	2.11	36	2.11
42	2.11	39	1.41	41	2.82	41	2.82
44	3.52	42	2.82	52	2.82	52	2.82
46	4.93	46	4.93	55	6.34	55	6.34
48	5.64	52	7.75	57	7.75	57	7.75
52	7.75	53	8.46	60	9.16	60	9.16
55	9.16	58	11.98	62	9.87	62	9.87
57	10.57	60	14.10	67	10.57	67	10.57
62	11.28	62	14.80	69	10.57	69	10.57
66	14.80	64	14.80	76	11.28	76	11.28
68	15.51	67	16.21	78	11.98	78	11.98
70	15.51	69	16.21	81	11.98	81	11.98
76	16.21	71	16.92	85	12.69	85	12.69
79	16.21	73	16.92	90	13.39	90	13.39
88	16.92	76	16.92	92	13.39	92	13.39
95	16.21	79	16.92	97	13.39	97	13.39
97	15.51	82	16.92	100	14.10	100	14.10
100	14.80	87	16.21	103	12.69	103	12.69
104	14.80	94	15.51	107	13.39	107	13.39
107	14.10	100	14.80	111	12.69	111	12.69
110	13.39	105	14.10	113	12.69	113	12.69
112	13.39	110	13.39	115	11.98	115	11.98
115	12.69	116	12.69	116	11.28	116	11.28
118	11.98	119	11.28	120	10.57	120	10.57
120	11.98	122	10.57	128	10.57	128	10.57
122	11.28	124	9.87	130	9.87	130	9.87
125	10.57	130	9.16	135	9.16	135	9.16
130	9.87	134	8.46	140	8.46	140	8.46
133	9.16	137	7.75	142	7.75	142	7.75
136	8.46	143	7.05	146	7.05	146	7.05
141	7.75	151	6.34	150	7.05	150	7.05
150	6.34	154	5.64	152	6.34	152	6.34
153	5.64	159	4.93	158	5.64	158	5.64
155	5.64	163	4.23	160	3.52	160	3.52
160	4.93	171	3.52	163	2.82	163	2.82
167	4.23	173	2.82	167	2.11	167	2.11
170	3.52	182	2.11	170	2.82	170	2.82
176	2.82	187	1.41	173	2.11	173	2.11
184	2.11	192	0.70	175	0.00	175	0.00
191	1.41	203	0.00				
199	0.70						

APPENDIX B

RAW DATA OF GRAVIMETRIC ANALYSIS OF LIQUID GRIT SAMPLE

Table B 1: Influent Sample Analysis (TS, FS, VS)

Sample		Influent 1	Influent 2
Volume (ml)		24	25
Initial wt.(Wi) (gm)		31.1223	30.1518
Dried wt.(W_{105}) (gm)		31.1456	30.1761
Final wt.(W_{550}) (gm)		31.1361	30.1653
TS (mg/L)		971	972
FS(mg/L)		575	540
VS(mg/L)		396	432
Average Data	TS (mg/L)	971	
	FS(mg/L)	557	
	VS(mg/L)	414	
Standard deviation	TS (mg/L)	1	
	FS(mg/L)	25	
	VS(mg/L)	26	

Table B 2: Influent Sample Analysis (TSS, FSS, VSS)

Depth (m)		Control 1	Control 2	Influent 1	Influent 2
Volume (ml)		50	50	30	30
Initial wt. (Wi) (gm)		16.0616	14.3444	15.7398	15.6530
Dried wt. (W_{105}) (gm)		16.0616	14.3444	15.7468	15.6602
Final wt. (W_{550}) (gm)		16.0616	14.3444	15.7439	15.6572
TSS (mg/L)		0.00	0.00	233.33	240.00
FSS (mg/L)		0.00	0.00	138.07	141.18
VSS (mg/L)		0.00	0.00	95.27	98.82
Average Data	TSS (mg/L)	0.00			236.67
	FSS (mg/L)	0.00			139.62
	VSS (mg/L)	0.00			97.04
Standard deviation	TSS (mg/L)	0.0			4.7
	FSS (mg/L)	0.0			2.2
	VSS (mg/L)	0.0			2.5

Table B 3: Effluent Sample Analysis (TSS, FSS, VSS)

Depth (m)	0.00	0.00	0.15	0.15	0.30	0.30
Volume (ml)	30	30	30	30	30	30
Initial wt. (Wi) (gm)	15.0514	14.0516	16.3358	16.3466	16.4084	15.4122
Dried wt. (W_{105}) (gm)	15.0580	14.0582	16.3424	16.3529	16.4153	15.4192
Final wt. (W_{550}) (gm)	15.0554	14.0556	16.3400	16.3508	16.4123	15.4161
TSS (mg/L)	220.00	220.00	220.00	210.00	230.00	233.33
FSS (mg/L)	131.74	131.92	139.39	139.36	128.97	128.89
VSS (mg/L)	88.26	88.08	80.61	70.64	101.03	104.44
Average Data	TSS (mg/L)	220.00		215.00		231.67
	FSS (mg/L)	131.83		139.38		128.93
	VSS (mg/L)	88.17		75.62		102.74
Standard deviation	TSS (mg/L)	0.0		7.1		2.4
	FSS (mg/L)	0.1		0.0		0.1
	VSS (mg/L)	0.1		7.0		2.4

Table B 4: Effluent Sample Analysis (TSS, FSS, VSS)

Depth (m)	0.46	0.46	0.61	0.61	0.76	0.76
Volume (ml)	30	30	30	30	30	30
Initial wt. (Wi) (gm)	15.2193	17.2261	16.3564	16.3458	16.6203	16.6321
Dried wt. (W_{105}) (gm)	15.2258	17.2327	16.3636	16.3530	16.6276	16.6395
Final wt. (W_{550}) (gm)	15.2233	17.2301	16.3607	16.3501	16.6247	16.6365
TSS (mg/L)	216.67	220.00	240.00	240.00	243.33	246.67
FSS (mg/L)	132.53	132.47	142.01	142.04	145.71	146.01
VSS (mg/L)	84.14	87.53	97.99	97.97	97.62	100.66
Average Data	TSS (mg/L)	218.33		240.00		245.00
	FSS (mg/L)	132.50		142.02		145.86
	VSS (mg/L)	85.83		97.98		99.14
Standard deviation	TSS (mg/L)	2.4		0.0		2.4
	FSS (mg/L)	0.0		0.0		0.2
	VSS (mg/L)	2.4		0.0		2.1

Table B 5: Effluent Sample Analysis (TSS, FSS, VSS)

Depth (m)	0.91	0.91	1.07	1.07	1.22	1.22
Volume (ml)	30	30	30	30	30	30
Initial wt. (Wi) (gm)	14.7165	14.7335	16.7630	17.8255	15.6379	16.5826
Dried wt. (W_{105}) (gm)	14.7230	14.7401	16.7696	17.8319	15.6442	16.5886
Final wt. (W_{550}) (gm)	14.7203	14.7373	16.7670	17.8295	15.6417	16.5864
TSS (mg/L)	216.67	220.00	220.00	213.33	210.00	200.00
FSS (mg/L)	128.21	128.32	132.53	132.58	125.75	125.81
VSS (mg/L)	88.46	91.68	87.47	80.75	84.25	74.20
Average Data	TSS (mg/L)	218.33		216.67		205.00
	FSS (mg/L)	128.26		132.56		125.78
	VSS (mg/L)	90.07		84.11		79.22
Standard deviation	TSS (mg/L)	2.4		4.7		7.1
	FSS (mg/L)	0.1		0.0		0.0
	VSS (mg/L)	2.3		4.8		7.1

Table B 6: Effluent Sample Analysis (TSS, FSS, VSS)

Depth (m)	1.37	1.37	1.52	1.52	1.68	1.68
Volume (ml)	30	30	30	30	30	30
Initial wt. (Wi) (gm)	16.4373	16.4456	14.4560	15.0107	14.8251	15.7864
Dried wt. (W_{105}) (gm)	16.4440	16.4523	14.4631	15.0173	14.8318	15.7934
Final wt. (W_{550}) (gm)	16.4416	16.4499	14.4607	15.0154	14.8292	15.7905
TSS (mg/L)	223.33	223.33	236.67	220.00	223.33	233.33
FSS (mg/L)	143.28	143.31	157.46	156.78	136.18	136.22
VSS (mg/L)	80.05	80.02	79.20	63.22	87.15	97.11
Average Data	TSS (mg/L)	223.33		228.33		228.33
	FSS (mg/L)	143.30		157.12		136.20
	VSS (mg/L)	80.03		71.21		92.13
Standard deviation	TSS (mg/L)	0.0		11.8		7.1
	FSS (mg/L)	0.0		0.5		0.0
	VSS (mg/L)	0.0		11.3		7.0

Table B 7: Effluent Sample Analysis (TSS, FSS, VSS)

Depth (m)	1.83	1.83	1.98	1.98	2.13	2.13
Volume (ml)	30	30	30	30	30	30
Initial wt. (Wi) (gm)	15.6651	16.6882	15.9614	15.8557	16.0820	17.0816
Dried wt. (W_{105}) (gm)	15.6728	16.6959	15.9686	15.8632	16.0901	17.0897
Final wt. (W_{550}) (gm)	15.6694	16.6925	15.9657	15.8601	16.0869	17.0865
TSS (mg/L)	256.67	256.67	240.00	250.00	270.00	270.00
FSS (mg/L)	143.43	142.97	144.58	145.41	164.63	164.64
VSS (mg/L)	113.23	113.69	95.42	104.59	105.37	105.36
Average Data	TSS (mg/L)	256.67		245.00		270.00
	FSS (mg/L)	143.20		144.99		164.64
	VSS (mg/L)	113.46		100.01		105.36
Standard deviation	TSS (mg/L)	0.0		7.1		0.0
	FSS (mg/L)	0.3		0.6		0.0
	VSS (mg/L)	0.3		6.5		0.0

Table B 8: Effluent Sample Analysis (TSS, FSS, VSS)

Depth (m)	2.29	2.29	2.44	2.44	2.59	2.59
Volume (ml)	30	30	30	30	30	30
Initial wt. (Wi) (gm)	15.7098	15.5421	16.9772	15.6523	15.8787	14.8985
Dried wt. (W_{105}) (gm)	15.7176	15.5498	16.9853	15.6606	15.8864	14.9062
Final wt. (W_{550}) (gm)	15.7151	15.5474	16.9821	15.6572	15.8834	14.9032
TSS (mg/L)	260.00	256.67	270.00	276.67	256.67	256.67
FSS (mg/L)	175.65	175.54	161.68	162.21	155.56	155.60
VSS (mg/L)	84.35	81.13	108.32	114.46	101.11	101.07
Average Data	TSS (mg/L)	258.33		273.33		256.67
	FSS (mg/L)	175.59		161.94		155.58
	VSS (mg/L)	82.74		111.39		101.09
Standard deviation	TSS (mg/L)	2.4		4.7		0.0
	FSS (mg/L)	0.1		0.4		0.0
	VSS (mg/L)	2.3		4.3		0.0

Table B 9: Effluent Sample Analysis (TSS, FSS, VSS)

Depth (m)	2.74	2.74	2.90	2.90	3.05	3.05
Volume (ml)	30	30	30	30	30	30
Initial wt. (Wi) (gm)	15.9013	16.5476	16.1082	16.1315	15.9421	15.9400
Dried wt. (W_{105}) (gm)	15.9101	16.5561	16.1163	16.1397	15.9502	15.9481
Final wt. (W_{550}) (gm)	15.9059	16.5522	16.1130	16.1363	15.9470	15.9449
TSS (mg/L)	293.33	283.33	270.00	273.33	270.00	270.00
FSS (mg/L)	153.85	153.56	159.76	159.78	162.65	163.42
VSS (mg/L)	139.49	129.77	110.24	113.55	107.35	106.58
Average Data	TSS (mg/L)	288.33		271.67		270.00
	FSS (mg/L)	153.70		159.77		163.04
	VSS (mg/L)	134.63		111.89		106.96
Standard deviation	TSS (mg/L)	7.1		2.4		0.0
	FSS (mg/L)	0.2		0.0		0.5
	VSS (mg/L)	6.9		2.3		0.5

Table B 10: Effluent Sample Analysis (TSS, FSS, VSS)

Depth (m)	3.20	3.20	3.35	3.35	3.51	3.51
Volume (ml)	30	30	30	30	30	30
Initial wt. (Wi) (gm)	17.6307	17.6327	16.6825	16.6754	14.6779	14.6811
Dried wt. (W_{105}) (gm)	17.6386	17.6404	16.6907	16.6836	14.6853	14.6884
Final wt. (W_{550}) (gm)	17.6354	17.6374	16.6875	16.6804	14.6824	14.6856
TSS (mg/L)	263.33	256.67	273.33	273.33	246.67	243.33
FSS (mg/L)	157.68	156.66	167.69	167.66	149.49	148.97
VSS (mg/L)	105.65	100.01	105.64	105.67	97.17	94.37
Average Data	TSS (mg/L)	260.00		273.33		245.00
	FSS (mg/L)	157.17		167.67		149.23
	VSS (mg/L)	102.83		105.66		95.77
Standard deviation	TSS (mg/L)	4.7		0.0		2.4
	FSS (mg/L)	0.7		0.0		0.4
	VSS (mg/L)	4.0		0.0		2.0

APPENDIX C

RAW DATA OF SIEVE ANALYSIS OF SOLID GRIT SAMPLE

Sieve analysis of grit sample dried at 105^0C

Initial mass (gm) = 1224
Initial dry mass (gm) = 518
Moisture in Grit (%) = 57.68
Dry mass after washing (gm) = 502
Mass lost by washing (gm) = 16

Table C 1: Raw data of sieve analysis

Mesh number	Sieve size (μm)	Mass retained (gm)	% retained	Cumulative % retained	% Finer
4	4760	76	14.67	14.67	85.33
10	2000	92	17.76	32.43	67.57
20	850	128	24.71	57.14	42.86
30	594	36	6.95	64.09	35.91
40	420	54	10.42	74.52	25.48
70	210	90	17.37	91.89	8.11
100	150	14	2.70	94.59	5.41
200	74	8	1.54	96.14	3.86
Pan + washed		18	3.47	99.61	
Total		516	99.61		
Discrepancy		2		0.39	

Sieve analysis of grit sample ignited at 550^{0}C

Initial mass (gm)	= 1286
Initial dry mass (gm)	= 546
Moisture in Grit (%)	= 57.54
Dry mass after washing (gm)	= 530
Mass lost by washing (gm)	= 16
Mass after burning @ 550°C (gm)	= 322

Table C 2: Raw data of sieve analysis

Mesh number	Sieve size (μm)	Mass retained (gm)	% retained	Cumulative % retained	% Finer
4	4760	2	0.60	0.60	99.40
10	2000	8	2.41	3.01	96.99
20	850	40	12.06	15.07	84.93
30	594	34	10.25	25.32	74.68
40	420	58	17.48	42.81	57.19
70	210	126	37.98	80.79	19.21
100	150	26	7.84	88.63	11.37
200	74	16	4.82	93.45	6.55
Pan + washed		20	6.03	99.48	
Total		330			
Discrepancy		2		0.52	

APPENDIX D

STRESS CALUCLATION FOR PILOT-SCALE GRIT CHAMBER

The model tank was 2.41 m long (L_M), 427 mm wide (W_M) and 493 mm deep (D_M). The water column depth (H_M) was 386 mm. Clean water was considered as the working fluid for the model and the fluid density (ρ_M) was 998.29 kgm^{-3} at 20^0C.

Water pressure on the tank floor, $P_b = H_M \times \rho_M \times g = 3780$ Pa

Force exerted on tank bottom, $F_b = P_b \times L_M \times W_M = 3885$ N

Force exerted by water on the inlet/outlet walls, $F_{i/o} = W_M \rho_M g \int_0^{0.493} D_M dD = 509$ N

Force exerted by water on the side walls, $F_{side} = \rho_M g \int_0^{0.493} D_M dD = 2870$ N

Flexural stress on tank bottom, $\sigma_b = \dfrac{F_b \times L_M}{W_M \times (0.0191)^2} = 60$ MPa

Flexural stress on the inlet/outlet walls, $\sigma_{i/o} = \dfrac{F_{i/o} \times W_M}{D_M \times (0.0191)^2} = 1.2$ MPa

Flexural stress on the side walls, $\sigma_{side} = \dfrac{F_{side} \times L_M}{D_M \times (0.0191)^2} = 38.6$ MPa